J. Fluid Mech. (2003), *vol.* 477, *pp.* 19–49.
DOI: 10.1017/S0022112002003063 Printed in the United Kingdom

Numerical experiments on strongly turbulent thermal convection in a slender cylindrical cell

By ROBERTO VERZICCO[1] AND ROBERTO CAMUSSI[2]

[1]Politecnico di Bari, DIMeG and CEMeC, Via Re David 200, 70125, Bari, Italy

[2]Università di Roma 'Tre', DIMI, via della Vasca Navale 79, 00146 Roma, Italy

(Received 5 June 2002 and in revised form 15 September 2002)

Numerical experiments are conducted to study high-Rayleigh-number convective turbulence (Ra ranging from 2×10^6 up to 2×10^{11}) in a $\Gamma = 1/2$ aspect-ratio cylindrical cell heated from below and cooled from above and filled with gaseous helium ($Pr = 0.7$). The numerical approach allows three-dimensional velocity, vorticity and temperature fields to be analysed. Furthermore, several numerical probes are placed within the fluid volume, permitting point-wise velocity and temperature time series to be extracted. Taking advantage of the data accessibility provided by the direct numerical simulation the flow dynamics has been explored and separated into its mean large-scale and fluctuating components, both in the bulk and in the boundary layer regions. The existence of large-scale structures creating a mean flow sweeping the horizontal walls has been confirmed. However, the presence of a single recirculation cell filling the whole volume was observed only for $Ra < 10^9$–10^{10} and with reduced intensity compared to axisymmetric toroidal vortices attached to the horizontal plates. At larger Ra the single cell is no longer observed, and the bulk recirculation breaks up into two counter-rotating asymmetric unity-aspect-ratio rolls. This transition has an appreciable impact on the boundary layer structure and on the global heat transfer properties. The large-scale structure signature is reflected in the statistics of the bulk turbulence as well, which, taking advantage of the large number of numerical probes available, is examined both in terms of frequency spectra and of temperature structure functions. The present results are also discussed within the framework of recent theoretical developments showing that the effect of the aspect ratio on the global heat transfer properties at large Ra still remains an open question.

1. Introduction

Turbulent convection in fluid layers confined between two horizontal plates occurs when a sufficiently large temperature difference between the lower heated and the upper cooled plates, is established. The main dimensionless parameter governing this phenomenon, often referred to as Rayleigh–Bénard convection†, is the Rayleigh number (Ra), defined as

$$Ra = \frac{g\alpha\Delta h^3}{\nu k}, \tag{1.1}$$

where Δ and h denote the temperature difference between the plates and their separation distance respectively and g is the acceleration due to gravity. The fluid

† True Rayleigh–Bénard flow is only for fluid layers of infinite extent in the horizontal directions. However, the same name is often used for confined geometries.

properties are described by the parameters α, ν and k which are, respectively, the thermal expansion coefficient, the kinematic viscosity and the thermal diffusivity. The increase of Ra leads to the onset of convective motion and, for $Ra > Ra_T \simeq 10^6$, for the present $\Gamma = 1/2$ aspect-ratio cylindrical cell, a fully developed turbulent state is reached in the bulk (see e.g. Heslot, Castaing & Libchaber 1987). It should be pointed out that the exact value of Ra_T depends not only on the particular criterion selected to judge the onset of turbulence but also on the cell geometry and the Prandtl number $Pr = \nu/k$; however, for sufficiently high values of Ra every configuration eventually becomes turbulent.

Over the past few decades, great effort has been devoted to the study of convective turbulence in the fully developed condition (Siggia 1994) owing to the direct implications either for problems of engineering interest (heat exchangers in power plants or melting processes) or for natural phenomena (e.g. in the atmosphere, oceans and Earth's mantle). From a practical viewpoint, one of the main features of interest is the influence of the forcing parameter, Ra, upon the heat exchange properties of the flow. The latter are estimated in non-dimensional form through the Nusselt number (Nu) defined as

$$Nu = \frac{Hh}{\lambda \Delta}. \tag{1.2}$$

Here H denotes the heat per unit surface area transferred between the two plates and λ the thermal conductivity. Theories and experiments have suggested a dependence of Nu on Ra of the form

$$Nu = ARa^{\beta}, \tag{1.3}$$

although with possible corrections (as suggested by Grossmann & Lohse 2000). An overview of past and more recent results (see e.g. Chavanne *et al.* 2001, and references therein) suggests that the power law (1.3) cannot be considered as 'universal' because of the dependence of the coefficients A and β upon other non-dimensional parameters. As suggested by Wu & Libchaber (1992), these governing dimensionless groups are the Prandtl number (Pr), and the aspect ratio Γ defining the ratio between the lateral and vertical extent of the cell. The first parameter is related to the fluid properties while the second is introduced since, for practical purposes, most of the experiments and numerical simulations of Rayleigh–Bénard convection are conducted in laterally confined domains. It is found, however, that even when Pr and Γ are fixed, a dependence of the coefficients of (1.3) upon Ra is observed provided Ra is sufficiently large. It was indeed found experimentally by Castaing *et al.* (1989) and theoretically confirmed by Shraiman & Siggia (1990) that at large Pr ($Pr \geqslant 0.4$), β is constant and equal to about $2/7$. The so-called $2/7$ regime is however observed within a limited range of Ra and both the upper bound of existence of this regime and the magnitude of β at very large Ra still remain unclear since the β parameter is not a constant. Such uncertainties limit the applicability of relation (1.3) for accurate heat transfer predictions since, due to the large Ra of interest in practical applications, a small error in the β estimation leads to order-of-magnitude errors in the Nu prediction.

The effect of Ra on the magnitude of β at large Pr is related to a change of the turbulent flow properties occurring at large Ra either within the bulk or close to the lateral walls. The major physical phenomenon influencing such a behaviour is the formation of large-scale vortical structures generating a mean flow. It is commonly assumed that, provided Γ is not too small, the large-scale structure typical length scale is of the order of the cell height, thus introducing constant 'winds' sweeping the plates and generating viscous and thermal boundary layers. The presence of

large-scale structures has therefore important practical and theoretical implications because Nu, and therefore the overall heat exchange properties of the flow, is directly linked to the thermal boundary layer thickness and nature (laminar or turbulent).

The above discussion explains the interest in clarifying the nature of the large-scale vortical structures forming within the cell at large Ra. The assumption of a mean current close to the wall is the basis of the recent theoretical works by Grossmann & Lohse (2000, 2001) where a phase diagram in the (Ra, Pr)-plane is proposed. The different flow regimes correspond to various power laws or to a combination of them. The presence of a 'wind' sweeping the walls is postulated and it is argued that different regimes might occur depending on the relative weight of the viscous or temperature dissipation either in the bulk or in the wall region. The agreement between the theoretical predictions and the experimental results seems good concerning global quantities but the physical properties of the large-scale structures associated with the various regimes actually unclear. Previous numerical simulations (Camussi & Verzicco 1999) have shown that a large-scale recirculating structure filling the whole volume is indeed present in the case of a $\Gamma = 1$ cell. It is suggested by the experiments of Ciliberto, Cioni & Laroche (1996) that the large-scale flow does not have an influence in the regime characterized by $\beta = 2/7$. On the other hand, the recent work by Daya & Ecke (2001) clearly indicates that the large-scale structure topology depends on the cell geometry, which weakly influences the Nu vs. Ra dependence but strongly affects the statistics in the bulk. At $Ra \gg 10^7$, various experimental results, even though still contradictory, seem to suggest that the large-scale structures play a key role in defining different flow regimes. For $Ra > 10^{10}$ approximately, a transitional regime has been observed experimentally by Chavanne *et al.* (2001) in a $\Gamma = 0.5$ cell. It is argued that the large-scale mean flow induces a transition in the boundary layer from a laminar to a turbulent state. Such a transition is also suggested by Chavanne *et al.* (2001) and Roche *et al.* (2001) to theoretically justify the ultimate regime $Nu \sim Ra^{0.5}$ observed at very large Ra ($Ra > 10^{12}$) and predicted decades ago by Kraichnan (1962). Other results however seem to contradict such conclusions. As examples, the early experiments at very large Ra by Wu *et al.* (1990) and the more recent investigations by Glazier *et al.* (1999) and Ashkenazi & Steinberg (1999) do not exhibit a clear transition for $Ra > 10^{10}$. The absence of a transition is also confirmed by the experiments of Niemela *et al.* (2000), which cover a wide range of Ra (up to $Ra = 10^{17}$), the only difference with the experiment of Chavanne *et al.* (2001) being the size of the cell.

The contradictory results of these experiments shows that a physical picture of the large-scale structure properties in the very high Ra convective regime at large Pr is still far from clear. Indeed, the analysis of indirect experimental results pertaining the large-scale motion leads to different possible interpretations of the large-scale flow behaviour and to contradicting theoretical implications. The present work is an attempt to shed some light on this by a numerical simulation of the high-Ra regime in a $\Gamma = 0.5$ cell at $Pr = 0.7$. The main aim is to numerically replicate the above cited recent experiments by Chavanne *et al.* (2001) and Niemela *et al.* (2000) which even though adopting the same non-dimensional parameters (namely Γ and Pr), show different results. The three-dimensional direct numerical simulation provides physical insights correlated with the topology of the large-scale structures, and information on quantities of interest which cannot be measured by experiments (e.g. vorticity, temperature and velocity three-dimensional fields). The range of Ra analysed here, $2 \times 10^6 \leqslant Ra \leqslant 2 \times 10^{11}$, is sufficiently wide to examine the occurrence of a flow transition which is tracked either by the analysis of the three-dimensional fields and

of the boundary layers or by point-wise temperature and velocity temporal statistics obtained by non-intrusive numerical probes placed within the bulk and close to the walls. Global quantities, such as energy and temperature dissipation computed either in the bulk or within the wall region and the most relevant turbulence quantities, are also analysed and discussed within the framework of the most recent theoretical developments (in particular those by Grossmann & Lohse 2000). We wish to stress that the present work covers a range of Ra which, as far as we know, has never been reached in previous direct numerical simulations. However, numerical capabilities leave the study of the ultimate regime observed by Chavanne *et al.* (2001) at $Ra \gg 10^{11}$ still unaffordable and further analysis on this remains a task for future experimental works. The large Ra analysed in the present work poses strong resolution requirements to be satisfied in the numerical simulation and the details of the numerical approach adopted are given in the next section. Results are presented in § 3 covering the description and discussion of the mean flow character and of the thermal and viscous boundary layer properties. The analysis of the core turbulence properties and of relevant statistics computed from the numerical probes are also included in § 3. Final remarks and conclusions are given in § 4.

2. Numerical set-up

The flow investigated in this paper is that developing in a cylindrical cell of aspect ratio $\Gamma = d/h = 1/2$ heated from below and cooled from above with an adiabatic sidewall. All the surfaces are no-slip. This configuration replicates the experimental set-ups of Chavanne *et al.* (2001), Niemela *et al.* (2000) and Roche *et al.* (2001) that used gaseous helium close to the critical point as working fluid.

A sketch of the set-up is given in figure 1 where the positions of 'ideal probes' are indicated by circles; 20 azimuthally equi-spaced probes are located on each circle and these are ideal in the sense that they provide simultaneous point-wise measurements of temperature and of the three velocity and vorticity components. They are also ideal since their presence does not disturb the flow even though they are about 400. The output of each probe consists of time series of the sampled quantities (see figure 2) that are analysed in the same way as in the experiments.

The flow is solved by numerically integrating the three-dimensional unsteady Navier–Stokes equations with the Boussinesq approximation:

$$\frac{\mathrm{D}\boldsymbol{u}}{\mathrm{D}t} = -\nabla p + \theta \hat{\boldsymbol{x}} + \left(\frac{Pr}{Ra}\right)^{1/2} \nabla^2 \boldsymbol{u}, \quad \nabla \cdot \boldsymbol{u} = 0,$$

$$\frac{\mathrm{D}\theta}{\mathrm{D}t} = \frac{1}{(PrRa)^{1/2}} \nabla^2 \theta,$$

with $\hat{\boldsymbol{x}}$ the unity vector pointing in the opposite direction to gravity, $\boldsymbol{u}$ the velocity vector, p the pressure (separated from its hydrostatic contribution) and θ the non-dimensional temperature. The equations have been made non-dimensional using the free-fall velocity $U = \sqrt{g\alpha\Delta h}$, the distance between hot and cold plates h and their temperature difference $\Delta = T_h - T_c$; the non-dimensional temperature θ is defined $\theta = (T - T_c)/\Delta$ so that $0 \leqslant \theta \leqslant 1$.

The above equations have been written in a cylindrical coordinate frame and discretized on a staggered mesh by central second-order accurate finite-difference approximations; the resulting discretized system is solved by a fractional-step procedure with the elliptic equation inverted using trigonometric expansions in the azimuthal

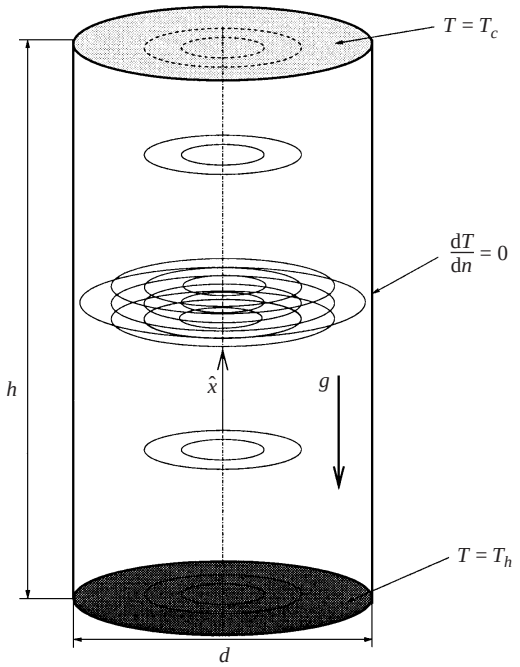

FIGURE 1. Sketch of the cell. All the surfaces are no-slip and the working fluid has $Pr = 0.7$. On each circle there are 20 azimuthally equi-spaced numerical probes.

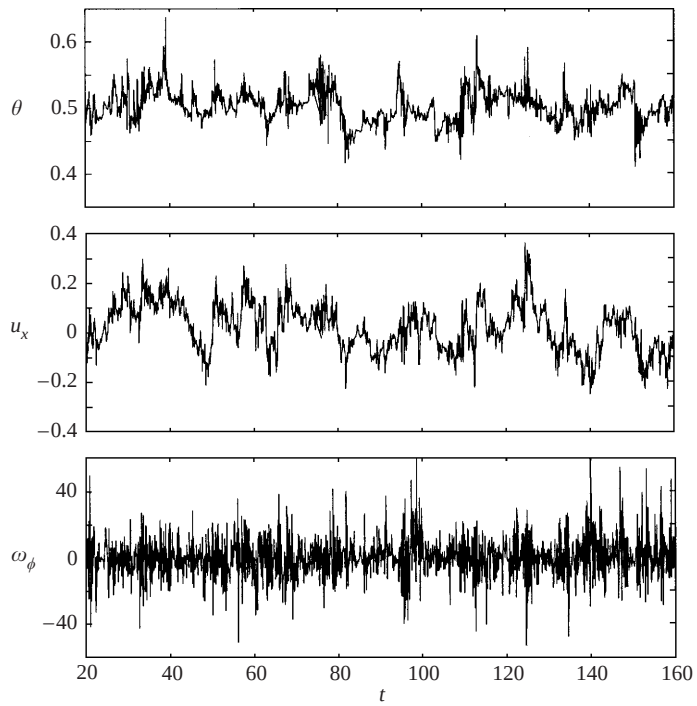

FIGURE 2. Example of the output of a numerical probe located halfway down the cell at $x/h = 0.5$ and $r/h = 0.0625$; $Ra = 2 \times 10^{10}$.

direction and the FISHPACK package (Swartzrauber 1974) for the other two directions. The time advancement of the solution is obtained by a hybrid low-storage third-order Runge–Kutta scheme. The numerical method is the same as that described in Verzicco & Camussi (1997) and Verzicco & Orlandi (1996) where further details of the numerical procedure can be found. The only relevant change with respect to the previous code is the presence of openMP directives allowing the use of multi-processor shared-memory computers.

The set of numerical experiments consists of six simulations at $Pr = 0.7$ and Ra in the range 2×10^6–2×10^{11}. The highest values of Ra may be beyond the present computing capabilities for a direct numerical simulation and a discussion of the resolution requirements is necessary in order to assess the quality of the results.

When performing a direct numerical simulation it must be ensured that the mesh size is of the same order (possibly equal or smaller) as the smallest flow scale η (the Kolmogorov scale) and, in the presence of solid surfaces, the viscous boundary layers must be adequately resolved. This means that within the boundary layer thickness δ_u a minimum number of gridpoints must be clustered and this condition is usually more restrictive than the previous one. The temperature field has similar resolution requirements with η_T (the Batchelor scale) and δ_θ (the thermal boundary layer thickness) instead of the viscous quantities. The above constrains must be satisfied simultaneously and therefore the most restrictive must be assumed. Usually the limitations on η and δ occur in different flow regions (the former in the bulk and the latter close to solid walls) therefore the use of a non-uniform grid is desirable. Accordingly, in this study the grid is non-uniform in the vertical and radial directions with the cells clustered close to the horizontal plates and close to the vertical sidewall in order to properly resolve the thermal and viscous boundary layers; in both cases the stretching function is an hyperbolic tangent.

For $Pr \leqslant 1$ flows $\eta \leqslant \eta_T$ and according to Grötzbach (1983) a reasonable estimate for the Kolmogorov scale is $\eta/h \simeq \pi(Pr^2/RaNu)^{(1/4)}$ which, combined with an appropriate correlation for the Nusselt number readily yields an estimate for η. Although the results by Chavanne *et al.* (2001) and Niemela *et al.* (2000) do not agree perfectly for all the values of Ra, the relation $Nu \simeq 0.124Ra^{0.309}$ fits the data reasonably well in the range of our interest and it is sufficiently accurate for our purposes. This fit has been used to compute the value of η and the results are given in table 1 together with the mesh size for comparison. In addition, since we are performing three-dimensional numerical simulations we can compute the kinetic energy dissipation rate ϵ from which the Kolmogorov scale can be directly computed by $\eta = (\nu^3/\epsilon)^{(1/4)}$; these values are also reported in table 1 for comparison. Note that the quality of the resolution is not always the same and that for the highest values of Ra the maximum grid size is slightly larger than η. This is because of the limited computing power; however that this resolution was enough to give accurate results was shown by grid refinement checks as discussed at the end of this section.

It is worth noting that since the energy dissipation rate $\epsilon = \sqrt{Pr/Ra}|\boldsymbol{\nabla u}|^2$ is a function of the vertical coordinate x, η will also depend on x. As will be shown in a later section, η is approximately constant in the bulk of the flow and decreases within the boundary layers. Inside the boundary layers, however, the resolution requirements based on their thickness is more restrictive than that required by η. As a consequence η will be evaluated halfway between the plates ($x/h = 0.5$), being representative of the resolution requirement in the bulk. Similar arguments and the same conclusions apply to the Batchelor scale η_θ the temperature variance dissipation $N = \sqrt{1/(PrRa)}|\boldsymbol{\nabla}\theta|^2$ and the thermal boundary layer thickness. We wish to stress that in this context

Ra	η/h estim.	η/h comp.	δ_θ/h estim.	δ_θ/h comp.	$N_\theta \times N_r \times N_x$	$\Delta_{\min}$	$\Delta_{\max}$
2×10^6	0.038	0.0392	0.0455	0.0312	$65 \times 49 \times 129$	0.0039	0.0078
2×10^7	0.018	0.0185	0.0223	0.0163	$97 \times 49 \times 193$	0.0010	0.0076
2×10^8	0.009	0.0088	0.0109	0.0090	$97 \times 49 \times 193$	0.0010	0.0076
2×10^9	0.0040	0.0039	0.0054	0.0050	$129 \times 65 \times 257$	0.0008	0.0057
2×10^{10}	0.0018	0.0019	0.0026	0.0018	$129 \times 97 \times 385$	0.00027	0.0048
2×10^{11}	0.0009	0.0010	0.0013	0.0011	$193 \times 129 \times 513$	0.00014	0.0036

TABLE 1. Variation of the Kolmogorov scale and thermal boundary layer thickness with Rayleigh number; 'estim.' are the values obtained by *a priori* estimates, 'comp.' are the values computed by the simulation. The minimum and maximum cell sizes are also reported in order to show the adequacy of the spatial resolution.

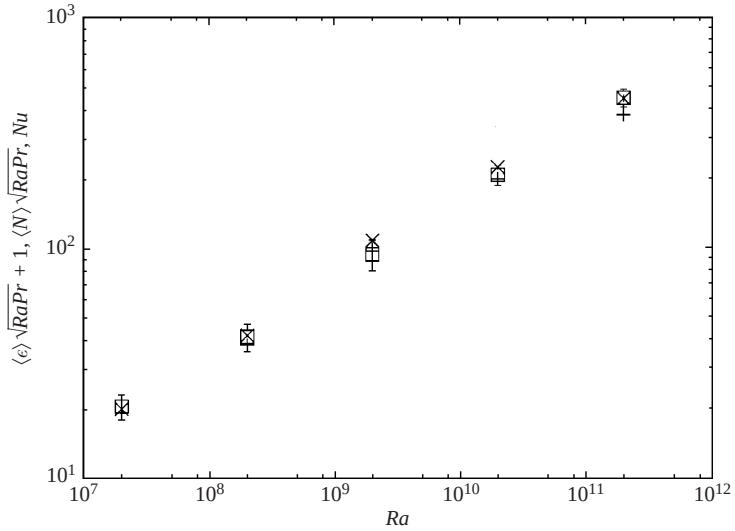

FIGURE 3. Comparison of the Nusselt number with the scaled dissipations as a verification of the consistency relations: $\times$, $\langle N\rangle\sqrt{RaPr}$; $+$, $\langle\epsilon\rangle\sqrt{RaPr}+1$; $\square$, Nu.

ϵ and N are the *local* dissipations only averaged in time and in the azimuthal direction; these are different from their global counterparts $\langle\epsilon\rangle$ and $\langle N\rangle$ averaged in time and over the whole fluid volume. The latter must satisfy the consistency relations $\langle\epsilon\rangle = (Nu-1)/\sqrt{RaPr}$ and $\langle N\rangle = Nu/\sqrt{RaPr}$ which have been verified in figure 3 as a further validation of the numerical results.

Concerning the boundary layer thickness, δ_u and δ_θ decrease with Ra at different rates and for $Pr = 0.7$ a cross-over can occur in $\Gamma = 1$ cells (Verzicco & Camussi 1999). However, for the present flow configuration ($\Gamma = 0.5$) $\delta_\theta < \delta_u$ and the former can be safely estimated by $\delta_\theta \simeq h/2Nu$. This means that the total temperature difference Δ is supported totally by the two thermal boundary layers while the temperature in the bulk is approximately uniform and equal to $(T_h + T_c)/2$. This estimate for δ_θ was used *a priori* to cluster the gridpoints in the boundary layer; a minimum number of six cells within the thermal boundary layer with the first gridpoint around $\delta_\theta/8$ was found to give accurate results without wasting computational resources. Of course,

we also used the data of the simulation to measure δ_θ and δ_u directly and to check *a posteriori* the resolution; these data are reported in table 1.

Two objections could be made to the above arguments: the first is that the estimates for η and δ_θ are only based on order-of-magnitude reasoning and there might be numerical prefactors changing their effective values; second, if a numerical simulation is under-resolved, the results for η and δ_θ are wrong, and therefore comparing these values with the estimates might give the misleading impression that the simulation is resolved.

Indeed the only truly reliable test to assess the quality of the results is a grid refinement check in which a flow is simulated with different grids and the results are checked against each other. On the other hand the simulations at the highest values of Ra already stretched our available computing capabilities and simulations on finer grids were not possible.

As a compromise we selected a case that could be simulated on over-resolved meshes and by systematically reducing the grid the minimum resolution requirements were identified. This was done by comparing the Nusselt number since Grötzbach (1983) suggests that this quantity is the most sensitive to the spatial resolution. The reference simulation is that of table 1 (case 2) at $Ra = 2\times10^7$ with the grid in the bulk 2.4 times smaller than the Kolmogorov scale, 10 gridpoints in the thermal boundary layer and the first point at $\delta_\theta/16$. For this case $Nu = 20.24 \pm 1.42$ while the value $Nu = 20.56 \pm 1.48$ was obtained on a grid with 5 points in the thermal boundary layer with the first point at $\delta_\theta/8$ and the mesh in the bulk four times larger than the Kolmogorov scale. Although whenever possible more-refined simulations were run, the above criteria have been fixed as minimum resolution requirement. The fact that a simulation with the mesh size four times η can still give accurate results is not very surprising when considering that, as mentioned by Pope (2000), η underestimates the size of the dissipative motions by more than a factor two and, according to Monin & Yaglom (1975), the transition separating the inertial range from the dissipative range occurs at about 10η.

A further indirect possibility for checking the adequacy of the numerical resolution is by computing the velocity and temperature spectra and verifying that in the dissipative range they decay exponentially without any build-up at the smallest scales (Jiménez *et al.* 1993). The correct behaviour of the spectra will be shown in § 3.4 where a comparison for the highest Ra is performed with experimentally measured analogous quantities (J. Niemela, personal communication).

An additional indirect way to assess the grid resolution is by computing the Nusselt number using different expressions. Resorting to the conductive and convective heat transfer definitions one can write $Nu = 1 + \sqrt{RaPr}\langle u_x\theta\rangle$ (Kerr 1996) where the angular brackets indicate an average over time and over the whole fluid layer. The Nusselt number can also be evaluated by computing directly the mean heat flux at the hot and cold plates $Nu = \overline{\partial\theta/\partial x}|_w$ where $|_w$ indicates that the derivative is evaluated at the wall and the overbar implies an average in time and over the plate surface. This latter definition requires an adequate spatial resolution of the thermal boundary layer while the former expression needs a correct estimation of the fluctuations in the bulk in order to evaluate the correlation $u_x\theta$. From preliminary simulations we observed that the values yielded by the two definitions agree only when the flow is well resolved either in the bulk or in the boundary layers therefore in each simulation this criterion was always used: the two Nusselt numbers were computed and each run was continued until the two definitions converged to the same value.

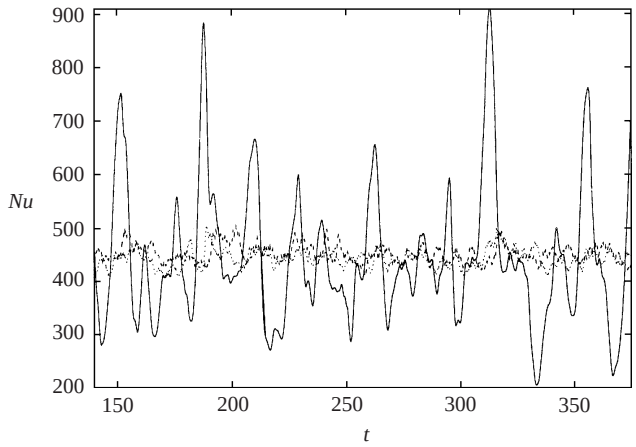

FIGURE 4. Time evolution of the Nusselt number according to the different definitions at $Pr = 0.7$, $Ra = 2 \times 10^{11}$: ———, integral in the bulk; · · · · · ·, – – – –, heat fluxes at the lower and upper plates.

As an aside we note that the long-term convergence of the first definition of Nu is due to the large-scale fluctuation of the mean temperature in the bulk which occurs on the same time scale as the integral quantities. This also provided a criterion to decide on the duration of each simulation since analogous statistics for turbulent quantities had to be computed (see figure 4). We wish to stress that this criterion prescribes that the duration of each simulation, in terms of large-eddy-turnover times T_L, is increased when the Rayleigh number is increased. In the present study, assuming a fluid particle to revolve inside the cell at a speed of the order of the free-fall velocity ($U = \sqrt{g\alpha\Delta h}$) along an elliptic path, we can estimate $T_L \simeq 2h/U$ yielding a simulation time of $T_{tot} = 100T_L$, $100T_L$, $100T_L$, $130T_L$, $165T_L$ and $220T_L$, respectively at $Ra = 2 \times 10^6$, 2×10^7, 2×10^8, 2×10^9, 2×10^{10} and 2×10^{11}. All the statistical quantities averaged over such a large number of large-scale characteristic times can be considered converged also on account of the fact that only mean and r.m.s. quantities are investigated in this paper. Nevertheless, in Niemela *et al.* (2001) it has been shown that T_L is not the longest period in the flow since a 'mean wind' reversal is observed that at $Ra = 1.5 \times 10^{11}$ occurs about every 2500 s. Even though the phenomenon was observed in a $\Gamma = 1$ cylindrical cell it is certainly possible that the same reversals are experienced by the flow in the $\Gamma = 1/2$ cell. In this respect the numerical simulation is useless since for a cell of $h = 50$ cm (like that of Niemela *et al.* 2001) filled with gaseous helium at $T = 4.2$ K and $\rho = 0.605\,\mathrm{Kg\,m^{-3}}$, with the fluid properties $\alpha = 0.238\,\mathrm{K^{-1}}$, $\nu = 2.1 \times 10^{-6}\,\mathrm{m^2\,s^{-1}}$ and $\kappa = 3.15 \times 10^{-6}\,\mathrm{m^2\,s^{-1}}$, it turns out that at $Ra = 2 \times 10^{11}$ a period of 220 large-eddy-turnover times corresponds to only 95.63 s. This implies that not every feature related to these reversals is captured by the numerical simulation, nor, therefore, the effects of the reversals on the flow statistics. It must be noted, however, that a recent paper by Sreenivasan, Bershadskii & Niemela (2002), has shown that the sidewall conductivity plays a significant role in the mean flow reversal through the thermal equilibrium of the corner eddies. In particular it was shown that at $Ra = 1.5 \times 10^{11}$ in a $\Gamma = 1$ cylindrical cell at $Pr = 0.7$ the mean wind had two equally probable directions while for smaller values of Ra the mean wind had a preferred state. In contrast, by reducing the sidewall conductivity the threshold value of Ra for the equi-probability of the two recirculation directions increased. Since in this paper the sidewall is perfectly adiabatic we expect, in the limited evolution

period which we could simulate, the mean wind to remain essentially in one direction even at the highest Rayleigh number (2×10^{11}).

Before concluding this section we note that the high-Ra conditions attained in this study are mainly due to the particular geometry of the domain. Given the low aspect ratio of the cell, the fluid volume contained in the domain is $V = h\pi d^2/4 \simeq 0.196h^3$; in contrast in a truly Rayleigh–Bénard problem, in which the horizontal dimensions of the domain are at least $l = 4h$–$6h$ (Kerr 1996) the flow volume would be $V = l^2h = 16h^3$–$36h^3$ and maintaining the same resolution as in this study would be impossible in practice.

3. Results

3.1. *The mean flow*

An important feature of this flow is the presence of large-scale structures whose characterization is important owing to the possible induction of constant 'winds' sweeping the plates and producing viscous and thermal boundary layers. The identification of the large-scale motion is also important because in laboratory experiments, owing to technical difficulties in the velocity measurements, these structures are conjectured from indirect evidence, such as correlating signals from two neighbouring temperature probes. Direct velocity measurements, on the other hand, are necessary in order to assess the existence of the postulated structure, to evaluate its strength and to separate the mean flow from velocity fluctuations.

A first simple way to detect the presence of the mean flow is by instantaneous flow visualizations like those of figures 5–7 where we report vertical and horizontal sections of temperature and vertical velocity for different Rayleigh numbers.

In many experimental analyses, assuming an analogy with the flow in the $\Gamma = 1$ cylindrical cell (for which a large body of literature is available), the presence of a unique large-scale recirculation completely filling the cell has been assumed and the velocity distribution induced by this structure used to interpret the temperature measurements.

From the panels of figures 5–7 we can see that the scenario is considerably more complex, with a mean flow structure which depends on the Rayleigh number and the unique large-scale recirculation which only appears for the lower values of Rayleigh number with limited intensity. The mean flow consists, in fact, of the superposition of two counter-rotating toroidal rings attached to the horizontal plates and the large-scale recirculation (figure 8*a*). The rings are axisymmetric and cause the fluid at the hot (cold) plate to raise (descend) along the lateral wall and to descend (raise) at the cell axis. This motion induces boundary layers which are thinnest at the centre of the plate and thicken in the radial direction. In contrast, the big roll with its asymmetric velocity field sweeps the horizontal plates in a single direction, inducing boundary layers that thicken monotonically while spanning the plates across the cross-section aligned with the mean current.

The overall features of the mean flow are determined by the relative importance of the two structures through the formation of the boundary layers. We have observed that for the lowest values of Ra the axisymmetric toroidal rings dominate the wall regions with the asymmetric large roll only playing a role in the bulk by generating a hot rising current on one side of the cell and a cold descending counterpart on the other side. In the range $10^9 < Ra < 10^{10}$ a transition occurs such that the axisymmetric torii weaken and the large-scale elliptical recirculation breaks into two

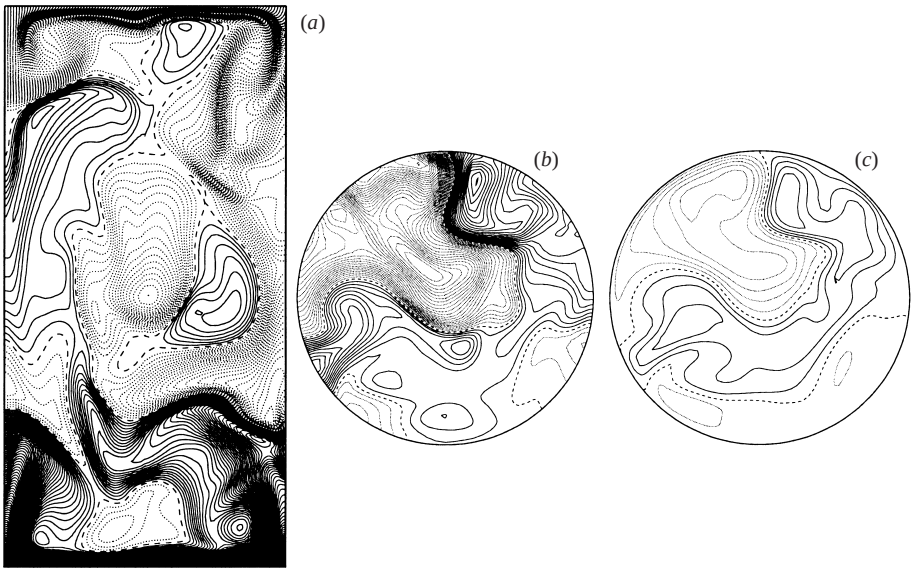

FIGURE 5. Instantaneous snapshots of temperature (a) in a vertical plane through the diameter and (b) in a horizontal plane midway between the plates; $\Delta\theta = 5 \times 10^{-3}$: ———, $0 \leqslant \theta < 0.5$; ·····, $0.5 > \theta \geqslant 1$; – – – –, $\theta = 0.5$. (c) As (b) but for the vertical velocity component; $\Delta u = \pm 0.05$: ———, $0 < u \leqslant 0.55$; ·····, $-0.55 \leqslant u < 0$; – – – –, $u = 0$. $Pr = 0.7$, $Ra = 2 \times 10^7$.

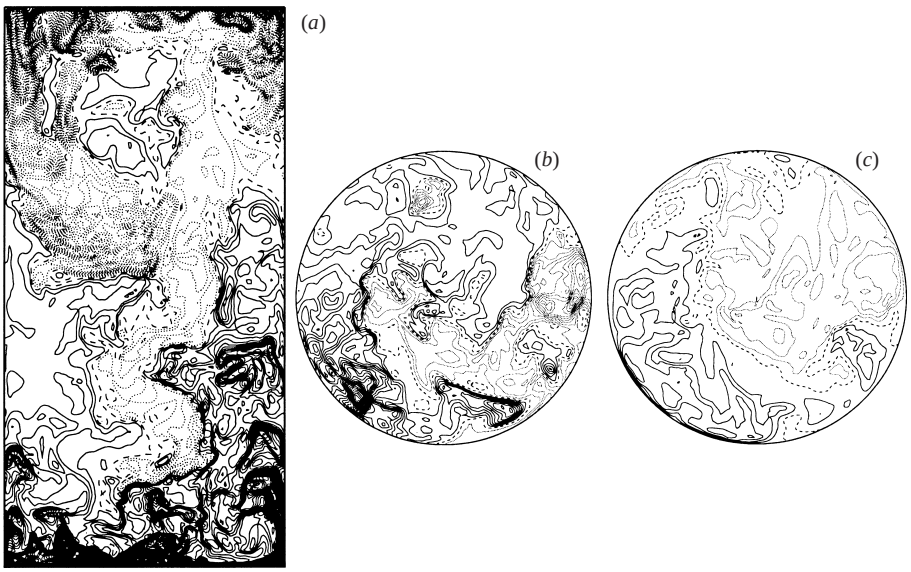

FIGURE 6. As figure 5 but for $Ra = 2 \times 10^9$.

unit-aspect-ratio counter-rotating recirculation rolls (figure 8b). These latter structures, sweeping the horizontal plates with constant currents, induce boundary layers different from those produced by the toroidal rings: this point will be quantitatively addressed in the next section. Another important effect of the counter-rotating rolls is that, acting like two counter-rotating flywheels, they bring into contact the fluid transported from the hot and cold plates at the cell centre thus producing a temperature jump in the bulk which affects the flow dynamics. This phenomenon has

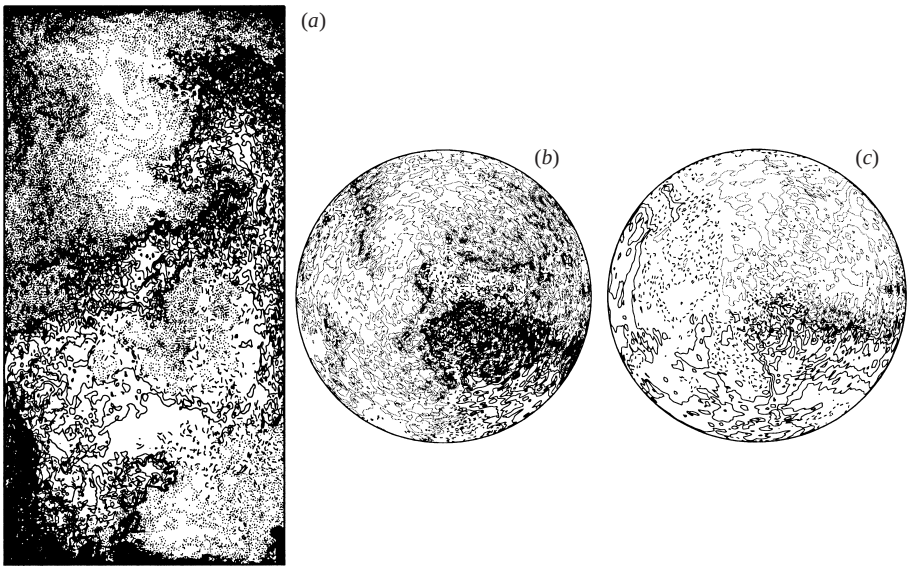

FIGURE 7. As figure 5 but for $Ra = 2 \times 10^{11}$.

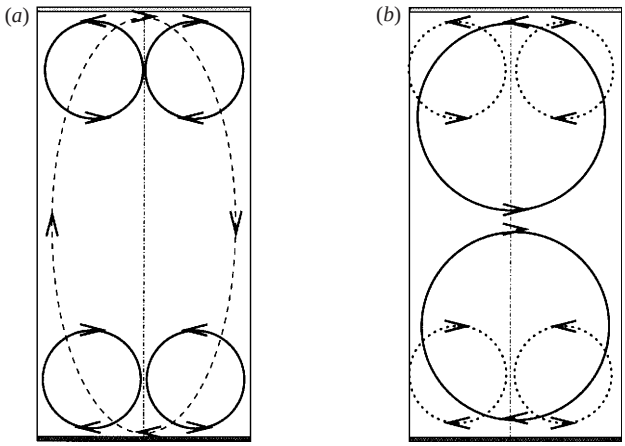

FIGURE 8. Sketch of the mean flow arrangement: (*a*) configuration for $Ra < 2 \times 10^9$, (*b*) $Ra \geqslant 2 \times 10^9$: ———, for the most intense structure; – – – –, for the weaker structure.

important implications for the decay of temperature and velocity spectra and will be discussed in § 3.4.

We wish to stress that the mean flow dynamics discussed above might appear impossible to conjecture from figures 5–7 since a single flow configuration does not provide enough information. In fact, the flow structure for every range of Rayleigh number has been deduced from the analysis of many snapshots of velocity and temperature fields together with animations in horizontal and vertical planes. Note, however, that the behaviours described only occur on the average since the largest scales experience reversals and azimuthal tilting with a statistical period of the order of 10–20 large-eddy-turnover times. In addition in the range $Ra = 2 \times 10^9$–2×10^{10} the two flow regimes described can co-exist with the large recirculation that randomly switches between the single-roll and counter-rotating-couple configuration. The dynamics

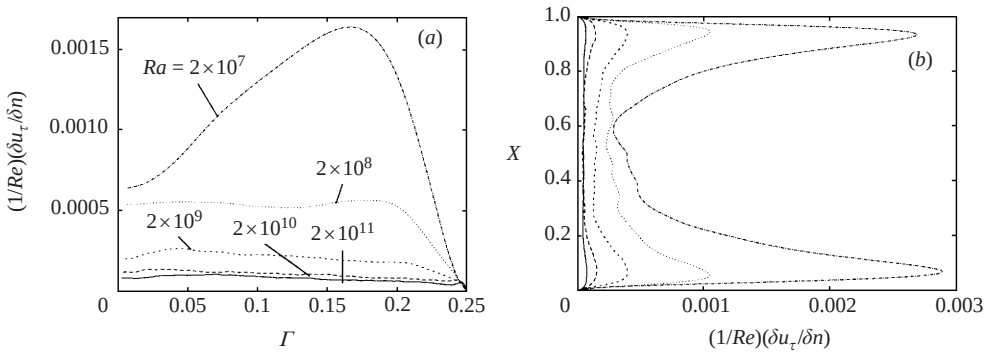

FIGURE 9. Mean wall-normalized velocity gradients: (*a*) radial profiles at the horizontal plate (the profiles are averaged in time and between the lower and upper plates), (*b*) vertical profiles at the sidewall (the profiles are averaged in time and in the azimuthal direction). ———, $Ra = 2 \times 10^{11}$; – – – –, $Ra = 2 \times 10^{10}$; - - - -, $Ra = 2 \times 10^{9}$; ·····, $Ra = 2 \times 10^{8}$; —·—, $Ra = 2 \times 10^{7}$; unless otherwise specified, the same line style has been used throughout the paper.

described is confirmed by the local friction coefficient profiles of figure 9 computed as the normalized (by $1/Re = \sqrt{Pr/Ra}$) wall-normal derivative of the tangential velocity. In particular, figure 9(*a*) shows the peak induced on the horizontal plate by the axisymmetric rings with amplitude that decreases with Ra, while at the highest values of Ra a constant value is observed as the signature of the more uniform wind induced by the asymmetric rolls (see figure 8). Similar information is obtained from figure 9(*b*) showing the profiles along the sidewalls; in this case also the peaks produced by the rings are evident before the transition and they tend to disappear for $Ra \geqslant 10^{10}$.

A more quantitative way of characterizing the mean flow is by determining its energy content. In particular, by taking a Fourier transform of the velocity field it is possible to decompose it into azimuthal modes n and then to compute the energy of each mode. Namely, if $\boldsymbol{u}(r, \theta, x)$ is the velocity field, taking the FFT in the azimuthal direction results in $\hat{\boldsymbol{u}}(r, n, x)$, with n the azimuthal wavenumber; the azimuthal energy modes are then obtained by integrating $\hat{\boldsymbol{u}}(r, n, x)\hat{\boldsymbol{u}}^*(r, n, x)$ over r and x, for each wavenumber n, $\hat{\boldsymbol{u}}^*$ being the complex conjugate of $\hat{\boldsymbol{u}}$. This decomposition is particularly significant since the $n = 0$ mode corresponds to the axisymmetric toroidal structures, the $n = 1$ mode contains the energy of the large-scale structures spanning the cell, while the $n \geqslant 2$ mode are the structures with n-fold azimuthal symmetry. In figure 10 we report the time evolution of the first ten energy modes for three Rayleigh numbers where we can see that even though the values fluctuate in time they attain stable mean values. It is worth noting that, owing to the polar-cylindrical frame of reference, every off-axis structure will also contain energy in the $n = 1$ mode; therefore its energy content can be ascribed not only to the large-scale recirculations but also to other asymmetric structures. In fact, in figure 10(*a*) we note that at $Ra = 2 \times 10^7$ the $n = 0$ and $n = 1$ modes have comparable energy and, since the velocity field is essentially dominated by the axisymmetric rings (figure 5), we can argue that the energy in the $n = 1$ mode is due to the background structures.

From the plots of figure 10 we extracted the percentage of energy contained in the $n = 0$ and $n = 1$ modes as a function of Ra and the results are reported in figure 11. We can see that at $Ra = 2 \times 10^7$ the energy content of the axisymmetric mode is the highest and it decreases to $Ra = 2 \times 10^9$ when it attains a steady value. On the other hand, the energy in the mode $n = 1$ increases with Ra up to $Ra = 2 \times 10^{10}$ and then

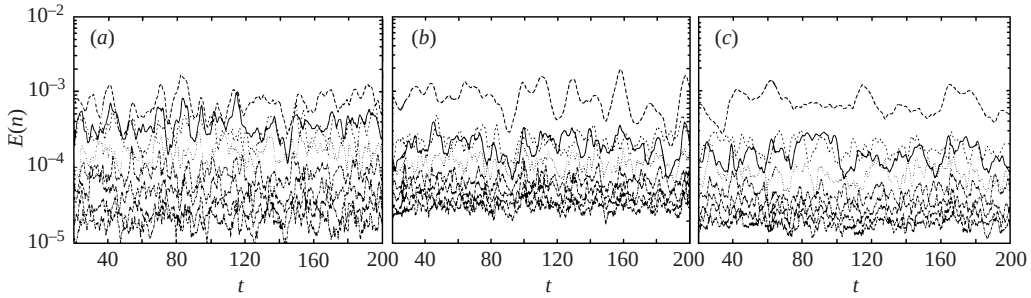

FIGURE 10. Time evolution of the azimuthal energy modes: (*a*) $Ra = 2 \times 10^7$, (*b*) $Ra = 2 \times 10^9$, (*c*) $Ra = 2 \times 10^{11}$: ———, $n = 0$ mode; – – –, $n = 1$ mode; - - - -, $n = 2$ mode; · · · · · ·, $n = 3$ mode; – · – · –, $n \geqslant 3$ modes.

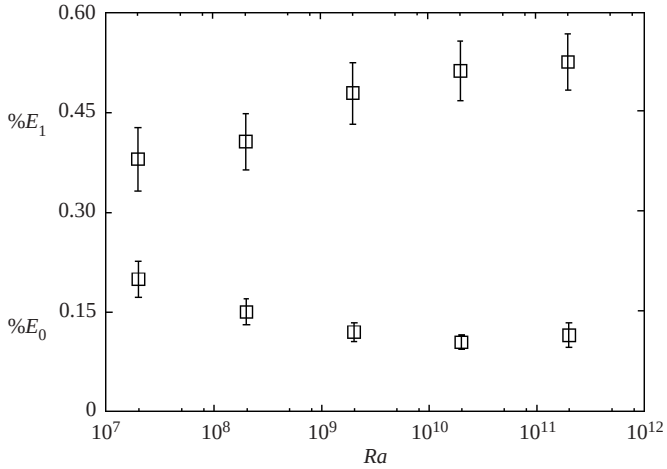

FIGURE 11. Percentage of the total kinetic energy contained by the $n = 0$ and $n = 1$ modes as a function of *Ra*.

saturates. This behaviour reinforces the picture of toroidal rings which weaken and asymmetric rolls which reinforce with *Ra* with a transition occurring in the range $10^9 < Ra < 10^{10}$. This is further confirmed by the behaviour of the averaged (in time) maximum vertical velocity with *Ra* (figure 12) showing an increase up to $Ra = 2 \times 10^{10}$ and then a constant value. We report for comparison the same data from Verzicco & Camussi (1999) who simulated the same flow in a $\Gamma = 1$ cylindrical cell; in that case only one single large-scale roll (without the toroidal rings) was observed with a circulation increasing with *Ra*. From the comparison it is immediately evident that in the present $\Gamma = 1/2$ cell the vertical velocity is smaller than that in the bigger aspect ratio cell. This is partly due to the dissipative effect of the lateral wall which is larger with respect to the cell volume in the smaller aspect ratio cell. Another reason for this difference is the topology of the mean flow. In the bigger aspect ratio cell, the unique large-scale roll allows the buoyancy forces to accelerate the fluid particle along the whole cell height (h). In contrast, in the high Rayleigh number regime, for the smaller aspect ratio cell the presence of two rolls halves this accelerating distance yielding smaller peak velocities.

The vertical profiles of the mean vertical velocity and temperature at the axis of the cell are reported in figure 13. The vertical velocity profiles (figure 13*a*) further confirm

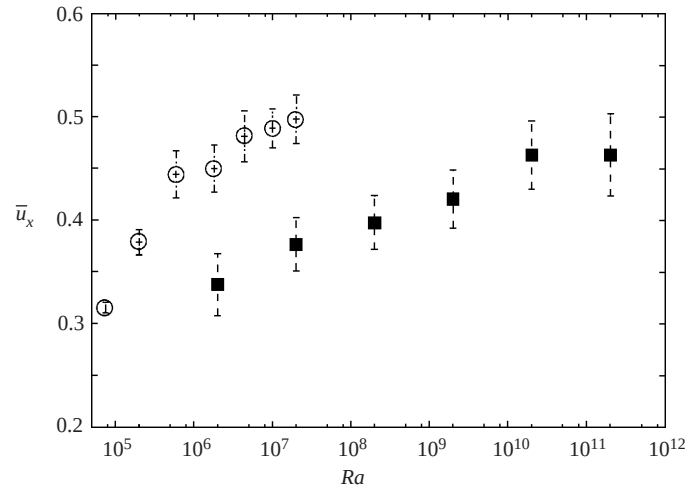

FIGURE 12. Time-averaged peak vertical velocity vs. Ra: ■, $\Gamma = 1/2$ cell; ○, $\Gamma = 1$ cell. The error bar is the size of the r.m.s. of the signal.

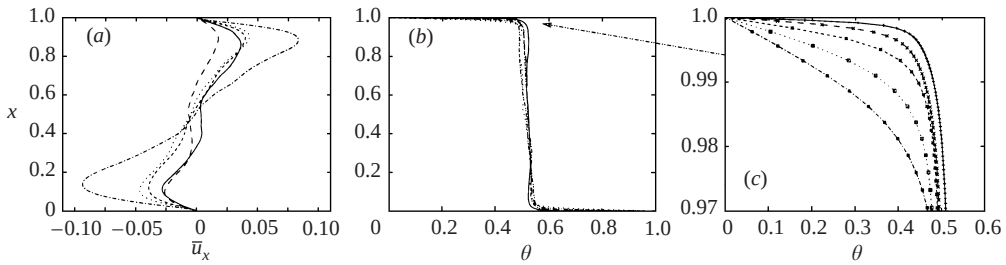

FIGURE 13. Mean vertical profiles of (*a*) vertical velocity and (*b*) temperature at the axis ($r = 0$): ——, $Ra = 2 \times 10^{11}$; – – – –, $Ra = 2 \times 10^{10}$; - - - -, $Ra = 2 \times 10^9$; · · · · ·, $Ra = 2 \times 10^8$; — · —, $Ra = 2 \times 10^7$. (*c*) A zoom of the upper thermal boundary layer with the spatial distribution of the gridpoints.

the presence of a transition in the mean flow configuration around $Ra = 2 \times 10^9$. In fact at $Ra = 2 \times 10^7$ the vertical velocity at the axis is negative for $x \leqslant h/2$ and positive for $x > h/2$, a clear signature of the axisymmetric rings (see figure 8*a*). As the Rayleigh number is increased the velocity magnitude decreases since the ring intensity decreases as well while the asymmetric single cell gives zero vertical velocity at the axis. For the highest values of Ra the asymmetric cells dominate the mean flow and, accordingly, the vertical velocity attains its minimum value close to the plates and it is zero at the centre of the cell. The profiles reported in figure 13(*b*) clearly show that the temperature remains about constant within the bulk while the temperature gradients are effective only within the thermal boundary layer (close up view is shown in figure 13*c*).

3.2. *Boundary layers*

The change in the features of the mean flow are also reflected in the dynamics of the boundary layers. In figure 14 we show the averaged r.m.s. vertical profiles of horizontal velocity and temperature which have peaks in the region close to the walls and a 'constant' value in the bulk of the flow. Assuming the distance of the peak r.m.s. from the wall as the boundary layer thickness we computed this value for the viscous and thermal layers and the results are given in figure 15. We can see that while the thermal boundary layer thickness steadily decreases with Ra with only a small

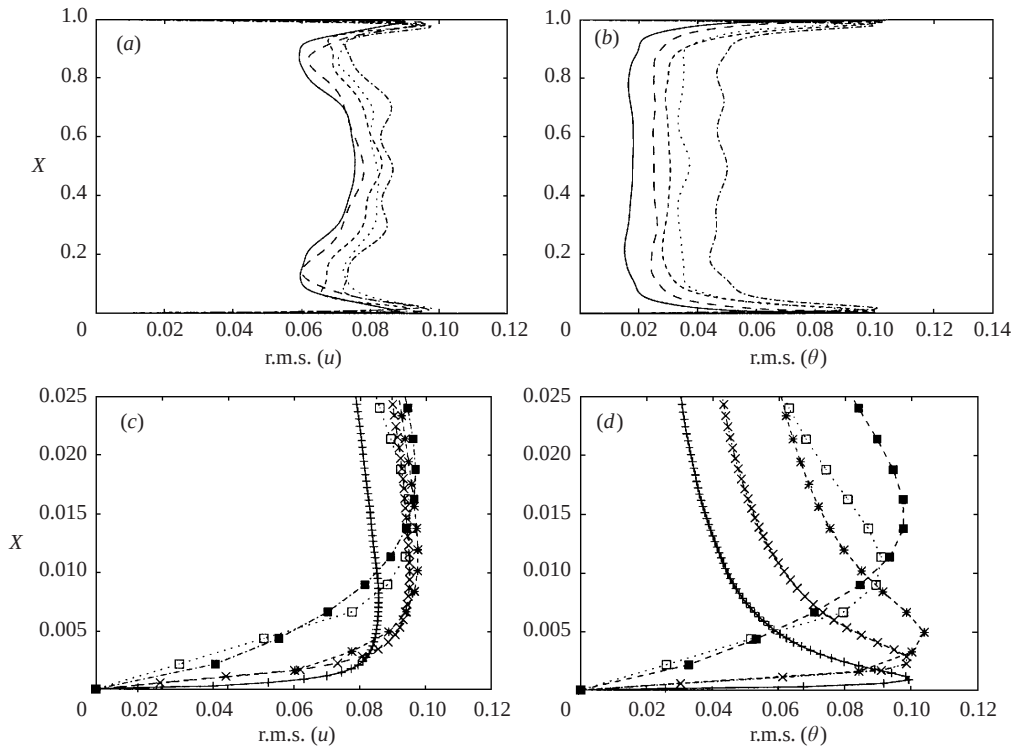

FIGURE 14. The same figure 13 but for the r.m.s. profiles. Panels (*c*) and (*d*) are enlargements of the lower wall regions with the gridpoint distribution.

bump around $Ra = 2 \times 10^9$, the viscous boundary layer also decreases but not with a constant slope, showing a clear thickening produced by the different mean flow. It is also observed that the thermal boundary layer thickness is always smaller than the viscous one and no cross-over is observed, in contrast with previous observations for $\Gamma = 1$ cells (Verzicco & Camussi 1999). We wish to stress that the transition mentioned is observed for the highest two Ra and therefore the possibility that this is a temporary change associated with the formation of the new structures and that at larger Ra the former scaling could appear again, cannot be ruled out.

Indirect experimental evaluations of the viscous boundary layer thickness also showed an evolution with Ra similar to the present one (see figure 4 of Belmonte, Tilgner & Libchaber 1994) and the observed behaviour was interpreted as an effect of a transition from a laminar to a turbulent regime (Belmonte *et al.* 1994; Chavanne *et al.* 2001). As further evidence of this transition $NuRa/(Pr^2Re^3)$ was evaluated as a surrogate of the friction coefficient C_f on the plates in order to show the different slope of C_f vs. Re pertaining to the laminar and turbulent regimes.

The analogy between the quantities C_f and $NuRa/(Pr^2Re^3)$ was obtained as follows: a uniform current with velocity U sweeping a flat plate of surface S exerts a force $F = \rho U^2 S C_f/2$ with a power $P = FU$. On the other hand, in the Rayleigh–Bénard cell the dissipated power is $P' = \rho V\langle 2\nu S_{ij}S_{ij}\rangle = \rho V\langle\epsilon\rangle = \rho V\nu(Nu-1)Rak^2/h^4 \simeq \rho V NuRa\nu k^2/h^4$, V being the volume of the cell. Assuming that all the dissipation in the cell occurs within the viscous boundary layers, by equating P and P' we obtain

$$C_f = NuRa\left(\frac{k}{\nu}\right)^2 \frac{\nu^3}{U^3h^3} = \frac{NuRa}{Pr^2Re^3}. \tag{3.1}$$

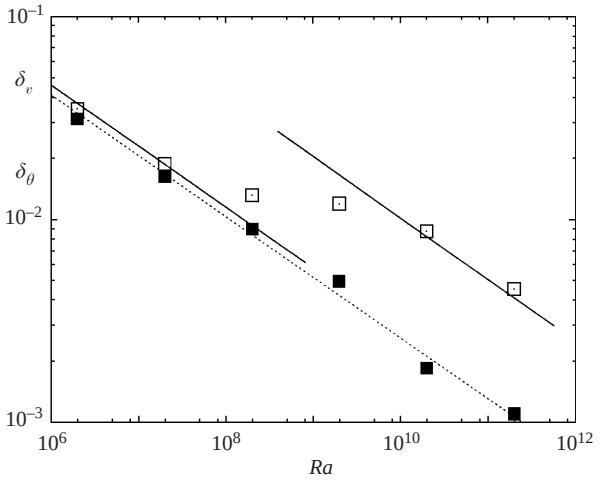

FIGURE 15. Viscous (□) and thermal (■) boundary layer thicknesses vs. *Ra*. All the lines are power laws $\delta \sim Ra^{-0.309}$.

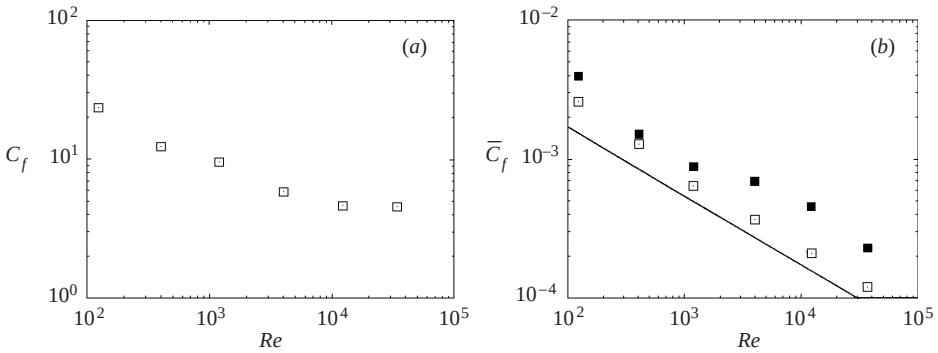

FIGURE 16. (*a*) 'Surrogate' and (*b*) real friction coefficients vs. *Re*. □, $\overline{C}_f$ computed over all solid surfaces; ■, $\overline{C}_f$ computed only over the horizontal plates. The line in (*b*) is the power law $Re^{-1/2}$. The Reynolds number is computed using the r.m.s. of the velocity.

This quantity was computed using the data of the direct numerical simulation and compared with the friction coefficient $\overline{C}_f$ directly evaluated from the velocity gradients at the solid walls. It is important to note that, since P' denotes the power dissipated by the whole flow, $\overline{C}_f$ must be computed by averaging its value over all solid surfaces, including the sidewall. In figure 16(*b*) $\overline{C}_f$ is plotted using open symbols and the analogous quantity computed only on the horizontal plates is also reported for comparison.

It can be noted that the surrogate friction coefficient (figure 16*a*) indeed shows a change in the slope and the 'knee' occurs at $Re \simeq 7000$ which is the same value observed by Chavanne *et al.* (2001). The actual friction coefficient $\overline{C}_f$, in contrast, decreases with *Re*, eventually following a power law $Re^{-1/2}$ which is characteristic of the laminar boundary layers. The friction coefficient averaged only on the horizontal plates starts decreasing as $Re^{-1/2}$ but it exhibits a 'dislocation' around $Ra = 2 \times 10^9$ and then decreases with the same slope as in the low Reynolds number region. It must be observed that given the limited number of points before and after the transition the equal slopes might be coincidental; nevertheless the important observation is that

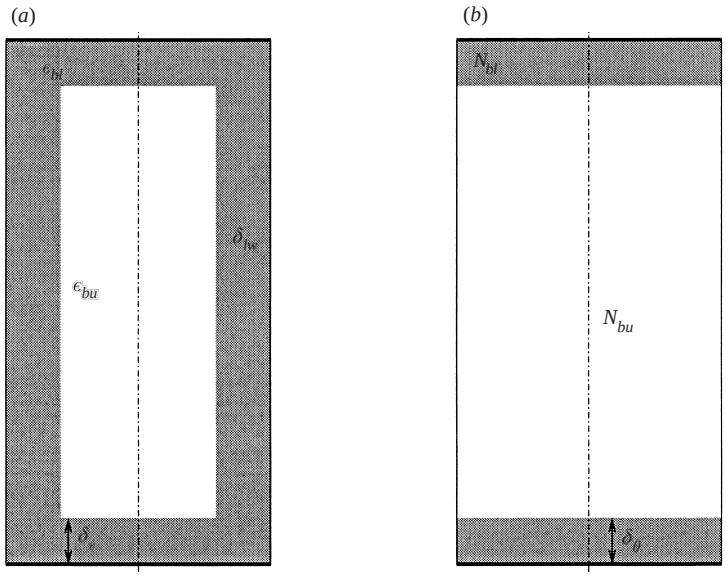

FIGURE 17. Sketch of the boundary layer/bulk region separation for (a) kinetic energy dissipation rate ϵ and (b) temperature variance dissipation rate N.

in this case the transition also is observed and that the friction coefficient continues to decrease with Re and does not attain a constant value like C_f. This indicates that the boundary layers remain laminar for this range of Rayleigh number and the absence of a transition is also confirmed by the r.m.s. profiles of figure 14 whose peak values are independent of the Rayleigh number. In fact, if a laminar/turbulent transition had indeed occurred within this regime an increase either in the velocity or in the temperature fluctuations should be observed.

We believe that the reason for the misleading behaviour of the surrogate C_f is that its definition relies on the key assumption that all the energy dissipated in the cell must be dissipated inside the viscous boundary layers.

In order for this point to be further clarified, the thermal and viscous dissipations have been computed from the spatial gradients of the three-dimensional velocity and temperature fields and the contributions coming from the bulk have been separated from those coming from the boundary layer regions. Since all the surfaces are no-slip, the boundary layer region for the kinetic energy dissipation rate ϵ includes the plates and the sidewall, whose boundary layer thickness is different from that of the plates (figure 17a). In contrast, owing to the adiabatic condition on the lateral wall the boundary layer region for the temperature variance dissipation rate N is only that coming from the horizontal plates (figure 17b). This is consistent with the distinction proposed by Grossmann & Lohse (2001) whose theory will be briefly compared with the present findings in the Conclusions.

The percentages of kinetic energy and temperature variance dissipation rates are reported in figure 18 as functions of Ra. It is shown that as the Rayleigh number is increased, the contribution to the dissipation from the bulk becomes dominant, thus contradicting the results of figure 14(a) based on the idea that the energy is entirely dissipated at the walls. It is also worth noting that, while for the temperature variance dissipation the boundary layers are only close to the horizontal plates, the velocity field also has a boundary layer in the lateral wall of the cell.

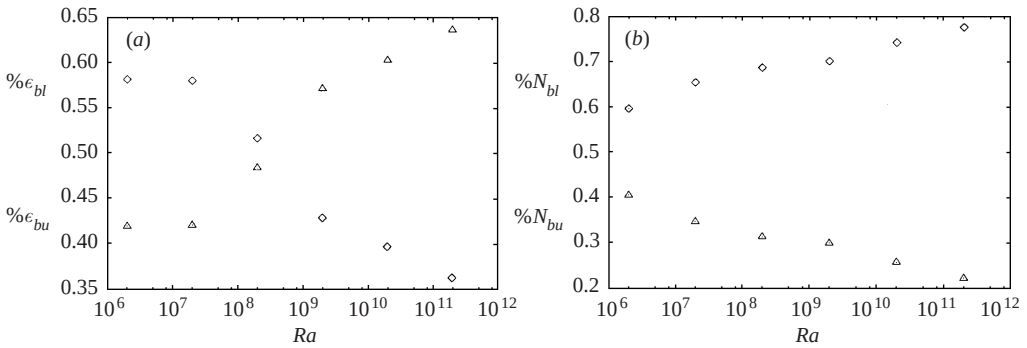

FIGURE 18. Percentage of (*a*) the kinetic energy dissipation rate and (*b*) temperature variance dissipation rate in the bulk and in the boundary layers vs. *Ra*; △, bulk contribution; ◇, boundary layer contribution.

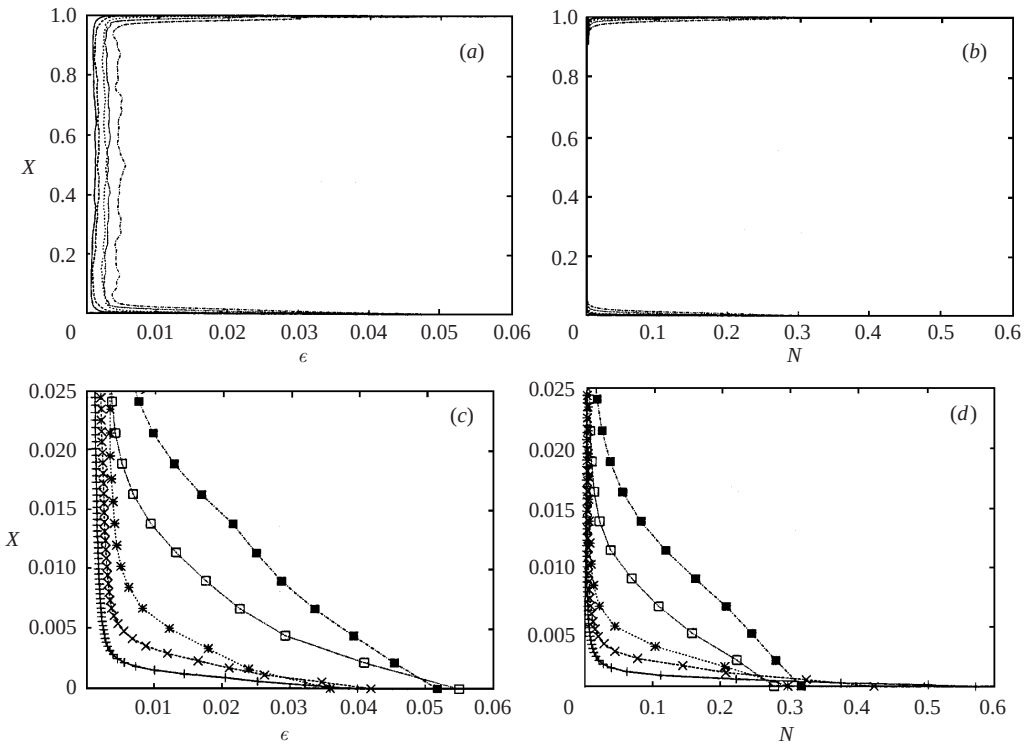

FIGURE 19. Mean vertical profiles of (*a*) kinetic energy dissipation rate and (*b*) temperature variance dissipation rate at the axis ($r = 0$); ——, $Ra = 2 \times 10^{11}$; – – – –, $Ra = 2 \times 10^{10}$; - - - -, $Ra = 2 \times 10^{9}$; · · · · ·, $Ra = 2 \times 10^{8}$; — · —, $Ra = 2 \times 10^{7}$. (*c*, *d*) A zoom of the lower boundary layers with the spatial distribution of the gridpoints.

From the spatial distribution of the dissipation, we have also computed the vertical profiles at the axis ($r = 0$) which are given in figure 19. Another important feature is the difference of values in the bulk and in the boundary layers for ϵ and N. Although ϵ attains the largest values in the boundary layer, the dissipation in the bulk is not negligible; thus, given the small volume of fluid of the boundary layers the bulk dissipation dominates (figure 19*a*). In contrast, for the temperature, N in the bulk is a negligible fraction of the wall value and essentially all the N is produced within the thermal boundary layers (figure 19*b*).

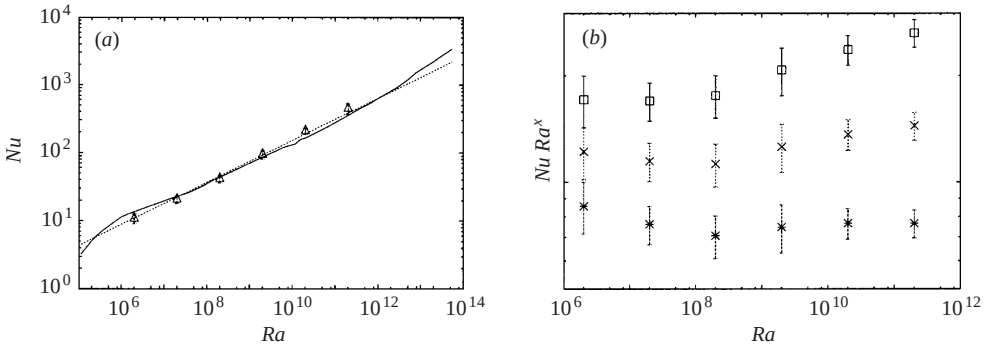

FIGURE 20. (*a*) Nusselt vs. Rayleigh numbers: symbols present results; ——, experimental data by Roche *et al.* (2001); – – – –, experimental fit $Nu = 0.124Ra^{0.309}$ by Niemela *et al.* (2000). (*b*) Compensated Nusselt number: □, $X = -2/7$; ×, $X = -0.309$; ∗, $X = -1/3$.

It must be noted that the separation of the dissipation contributions into bulk and boundary layer relies heavily on the boundary layer thickness definition; therefore the percentage values of figure 18 should be considered as indicative. Nevertheless, as noted in Kerr (1996, 2001) the thicknesses computed from the r.m.s. peaks show the slowest decrease with Ra, thus confirming that plots such as in figure 18 based on different boundary layer thickness definitions would give the same trends.

In figure 20 we report the non-dimensional heat transfer as a function of Rayleigh number with some experimental results for comparison. The data reported in figure 20(*a*) show that there is a substantial agreement with the experiments and that a clear change of slope in the Nusselt vs. Ra relation cannot be detected. However, when the Nusselt number is plotted in a compensated form (figure 20*b*) the slope before and after $Ra = 2 \times 10^9$ seems to change from the expected $2/7$ scaling to $1/3$ for $Ra > 10^9$. Nevertheless, given the error bars and the relatively limited (with respect to the experimental studies) Rayleigh number spanned by the simulations the above results have to be viewed with care and have only qualitative meaning. We wish to stress, however, that the error bars in figure 20 have been computed from the r.m.s. of the Nu fluctuations evaluated in the bulk (see figure 4) and they are of the order of 10%. On the other hand, in §2 we have seen that at $Ra = 2 \times 10^7$ when the resolution in the thermal boundary layer is decreased from 10 to 5 points Nu increases only by 1.2%. This suggests that if for a halved resolution the error doubled or even quadrupled it would be still of the order of 5% and therefore not large enough to induce a change of scaling. In addition, the simulations at $Ra = 2 \times 10^{10}$ and $Ra = 2 \times 10^{11}$ were indeed both resolved with 5 points in the thermal boundary layer and the deviation of Nu from the power law $Ra^{2/7}$ are of the order of 35% and 50%, respectively; therefore we tend to exclude the observed increased heat transfer being caused by lack of numerical resolution. The same conclusion is achieved when trying to distinguish between the power laws $Ra^{-0.309}$ and $Ra^{1/3}$; in fact by differentiating logarithmically the Nu values for the three highest values of Ra the exponent $\beta = 0.338$ is obtained while Nu at $Ra = 2 \times 10^{11}$ should be reduced by more than 13% to obtain the exponent $\beta = 0.309$.

3.3. *Core turbulence*

The flow region far from the solid walls ($0.3h \leqslant x \leqslant 0.7$ and $r \leqslant 0.3L_r$) is governed by nearly isotropic fluctuations whose dynamics can be characterized by investigating eventual scaling laws with Ra. Some representative scaling relations are reported in

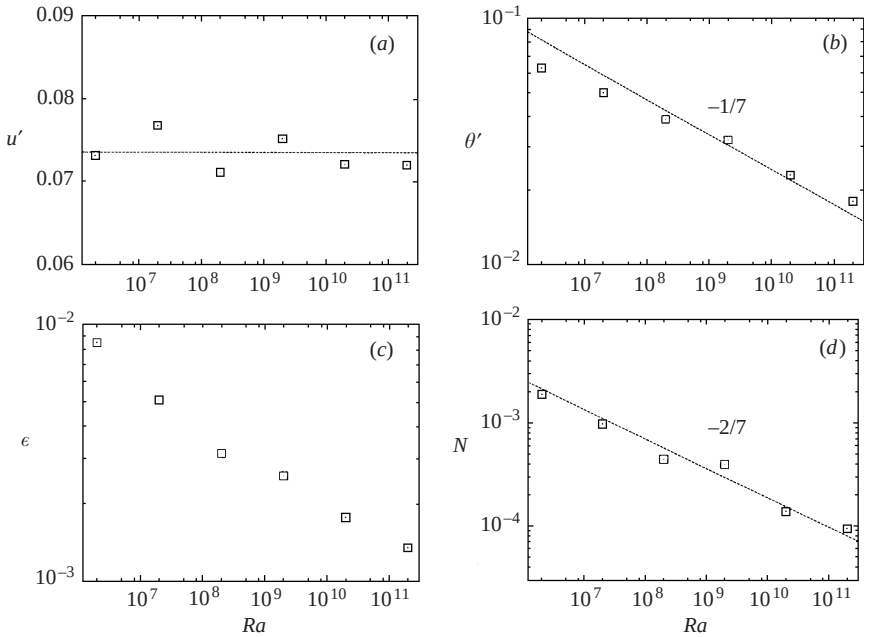

FIGURE 21. Statistics of turbulent quantities computed in the bulk ($0.3h \leqslant x \leqslant 0.7h$ and $r \leqslant 0.3L_r$).

figure 21; the upper panels report the r.m.s. of velocity and temperature fluctuations which have been obtained by averaging the three-dimensional data fields in the azimuthal direction and in time over the flow region $0.4h \leqslant x \leqslant 0.6h$ and $r \leqslant 0.08h$. When these quantities are plotted as function of Ra it is observed that $u' \sim$ const. even though, given the scatter of the data, a weak decrease with Ra cannot be ruled out. For the r.m.s. of the temperature, in this case also the signature of the mean flow transition is present with a 'dislocation' around $Ra \simeq 10^9$ and two regions with a power law decrease close to $\theta' \sim Ra^{-1/7}$ which has already been found in experiments by Wu (1991) and Niemela *et al.* (2000).

From the three-dimensional data fields the energy dissipation rate ϵ and the temperature variance dissipation rate N have been computed using the spatial gradients and the results are reported in figure 21(c, d). According to the turbulent nature of the flow one should expect $\epsilon \sim (u')^3 \sim$ const. and $N \sim u'(\theta')^2 \sim Ra^{-2/7}$, but only the latter prediction is confirmed by the measurements. On the other hand, recalling the definitions $\epsilon \approx (u')^3/\mathscr{L}$ and $N \approx u'(\theta')^2/\mathscr{L}_\theta$, with $\mathscr{L}$ and $\mathscr{L}_\theta$ the integral and temperature integral length scales, and relying on the results of figures 21(a) and 21(b), the above predictions can be correct provided $\mathscr{L}$ and $\mathscr{L}_\theta$ are constant with Ra. Once again, only the latter prediction is confirmed while the scaling of ϵ indicates a Ra-dependence of $\mathscr{L}$; in particular, since ϵ decreases with the integral scale $\mathscr{L}$ must increase with Ra.

Considering that an integral scale is a spatial dimension over which the phenomenon is forced, the above results are not surprising; in fact the maximum temperature difference is always at the distance between the plates and it is therefore reasonable to expect $\mathscr{L}_\theta \sim h$. In contrast the velocity integral scale $\mathscr{L}$ depends on the shape and strength of the large-scale vortices in the flow. According to the analysis in § 3.1 it is therefore reasonable that $\mathscr{L}$ increases with Ra since the large recirculations become

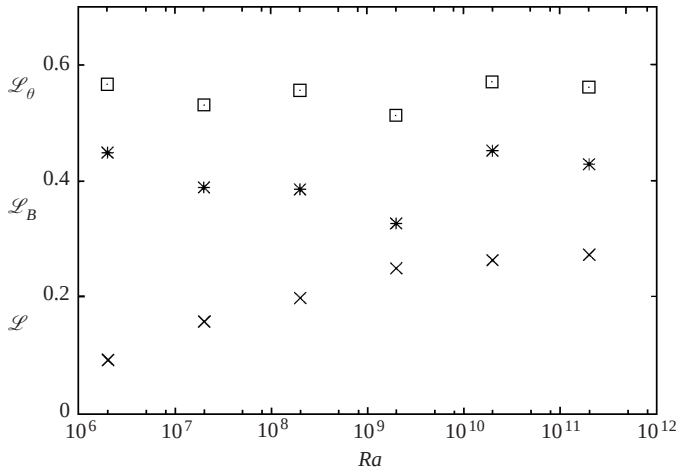

FIGURE 22. Velocity integral (+), temperature integral (□) and Bolgiano (∗) lengths vs. Rayleigh number. All lengths are made non-dimensional by the cell height h.

dominant with respect to the smaller toroidal structures. It is important to note that this behaviour cannot be asymptotic since an indefinite growth of $\mathscr{L}$ with Ra would eventually lead to $\mathscr{L} > h$ which is physically meaningless; this suggests a saturation in the increase of $\mathscr{L}$ to a fixed fraction of h corresponding to a saturation of the dimension and intensity of the large-scale structures. This conjecture is indirectly confirmed by the results of figure 12 where the averaged vertical velocity seems to attain a limiting value for $2 \times 10^9 \leqslant Ra \leqslant 2 \times 10^{10}$. Indeed, without the value at $Ra = 2 \times 10^{11}$ of figure 12 a different conclusion would be obtained, and therefore this point should be taken with caution; nevertheless, if we assume that the flow at aspect ratio $\Gamma = 1/2$ has the same behaviour as that at $\Gamma = 1$ a saturation in the velocity value could occur as indicated by the data for the latter cell.

The analysis of the integral lengths in convective turbulence assumes a particular relevance since there is a third quantity, the Bolgiano length, which introduces additional turbulence dynamics. Briefly, in standard turbulence the energy is injected at dimensions of the order of the integral scale and dissipated at the smallest (Kolmogorov) scales with only an inertial cascade in between. In convective turbulence, in contrast, the correlation between vertical velocity and temperature fluctuations can generate an additional energy injection at spatial scales of the order of $\mathscr{L}_B$ which is called the Bolgiano length. Of course, in order for this process to be physically realizable, $\mathscr{L} > \mathscr{L}_B > \eta$ and $\mathscr{L}_\theta > \mathscr{L}_B > \eta_\theta$ must hold for velocity and temperature, respectively.

The turbulent length scales have been computed from the dimensional estimates $\mathscr{L} \approx u'^3/\epsilon$, $\mathscr{L}_\theta \approx \theta'^2 u'/N$ and $\mathscr{L}_B \approx \epsilon^{5/4}/[(g\alpha)^{3/4} N^{3/4}]$ by averaging in time, in the azimuthal direction and over the radial distance $0 \leqslant r \leqslant d/6$, thus retaining only the dependence on the vertical coordinate x. The values in the bulk (shown in figure 22) have been obtained by vertically averaging the profiles over $0.4h \leqslant x \leqslant 0.6h$. Although only qualitatively, the variation of the scales in terms of Ra supports the above arguments on the variability limits of $\mathscr{L}$ and $\mathscr{L}_\theta$ for increasing Ra. It is also shown that even at the largest Ra attained in the present simulation $\mathscr{L}_B$ is always smaller than $\mathscr{L}_\theta$. As pointed out above, the interpretation of such results must be taken with care due to the variability of the scales in space and, in particular, of

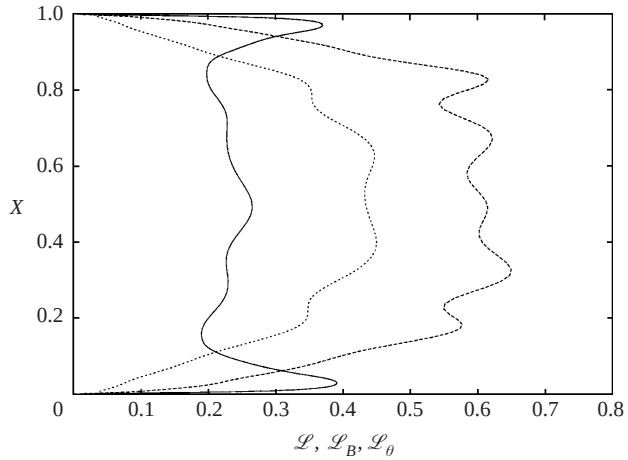

FIGURE 23. Velocity integral (——), temperature integral (– – – –) and Bolgiano (· · · · · ·) lengths as a function of the vertical coordinate at $Ra = 2 \times 10^{10}$. All lengths are made non-dimensional by the cell height h.

$\mathscr{L}_B$. In fact, looking at figure 19 it is clear that both ϵ and N depend on the vertical coordinate x and so do $\mathscr{L}$, $\mathscr{L}_\theta$ and $\mathscr{L}_B$. As an example, figure 23 reports the spatial variation of the lengths with x for one value of Ra showing the possibility of switching between Kolmogorov and Bolgiano dynamics depending on the distance from the plates.

We have seen, however, that the largest variations are located close to the boundaries while homogeneous and isotropic conditions are attained only in the core region where all the lengths are nearly constant. This allows the flow to be separated into two regions, the first dominated by the wall dynamics or boundary layer region and the second by developed turbulence or isotropic core region.

As a conclusion of this section it must be noted that the values of the scales $\mathscr{L}$, $\mathscr{L}_\theta$ and $\mathscr{L}_B$, being obtained on dimensional grounds, only give order of magnitude estimates while the exact values could be affected by numerical prefactors significantly different from unity. Nevertheless, the important point is that, according to their definitions, these lengths can evolve in a different way depending on the flow dynamics and they do not need to be a fixed fraction of the distance h between the plates.

3.4. *Frequency spectra and temperature structure functions*

Further details on the turbulence dynamics are obtained by the analysis of the frequency spectra computed by the Fourier decomposition of the time series sampled by the numerical probes. As indicated in figure 1 the different locations of the probes permitted us to analyse the bulk homogeneous region separately from the region of flow close to the lateral walls. In figure 24 the temperature spectra obtained from time series sampled within the homogeneous region at different Ra are reported. It is clearly shown that for increasing Ra the number of excited frequencies broadens. Figure 24(a) gives an indication that a fully turbulent state is already reached even at the lowest Ra considered here and that no preferred frequency modes are observed to prevail. It is also shown that for about $Ra \geqslant 2 \times 10^9$ the spectral decay follows a power law which, at $Ra = 2 \times 10^{10}$, extends for about two decades. A comparison between temperature and velocity spectra computed from the bulk probes at $Ra = 2 \times 10^{10}$ is reported in figure 25. Concerning the temperature behaviour (figure 25b), the reference power laws

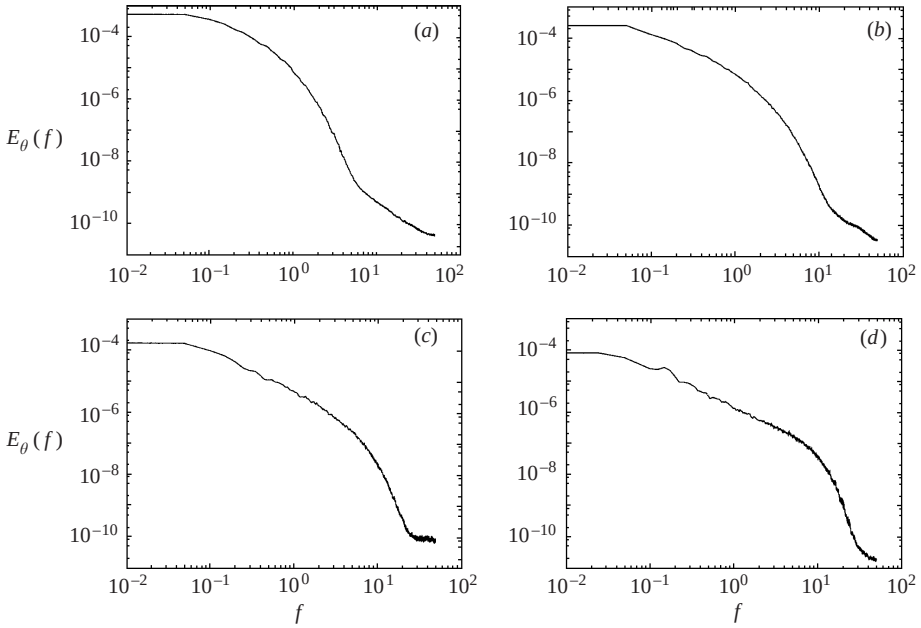

FIGURE 24. Temperature spectra in the bulk (all the probes with $0.4 \leqslant x/h \leqslant 0.6$ and $r/h \leqslant 0.1$): (*a*) $Ra = 2 \times 10^7$, (*b*) $Ra = 2 \times 10^8$, (*c*) $Ra = 2 \times 10^9$, (*d*) $Ra = 2 \times 10^{10}$.

reported in the figure clearly demonstrate that the scaling exponent of the measured spectrum is very close to $-7/5$. This result indicates that temperature fluctuations follow the so-called Bolgiano dynamics according to which the velocity spectrum should decrease with a $-11/5$ slope. However, a different behaviour is observed for the velocity fluctuations (figure 25*a*) which instead are characterized by the typical Kolmogorov scaling leading to a power law spectral decay with exponent $-5/3$. It should be stressed that the three spectra reported in figure 25(*a*) are computed from the three velocity components. The good collapse of the curves demonstrates that, as expected, turbulence is isotropic in the bulk.

Our original interpretation of the observed scalings considered the direct estimation of the integral and Bolgiano length scales characterizing temperature and velocity fluctuations. As was shown in figure 22, at $Ra \simeq 2 \times 10^{10}$ the result is $\mathscr{L} < \mathscr{L}_B$ and $\mathscr{L}_\theta > \mathscr{L}_B$ suggesting that the velocity spectrum follows the classical Kolmogorov scaling and the temperature spectrum the Bolgiano dynamics. This is, however, inconsistent with the Bolgiano argument since it is based on balancing $u^3/r \sim g\alpha\theta u$ and $u\theta^2/r \sim N$ from which $u \sim r^{3/5}$ and $\theta \sim r^{1/5}$ is obtained. In contrast a mixed Kolmogorov–Bolgiano scaling for velocity and temperature would give $u \sim r^{1/3}$ and $\theta \sim r^{1/5}$ which, when substituted in the above relation for N yield $u\theta^2/r \sim N \sim r^{-4/15}$; this is inconsistent with the initial hypothesis of N independent of r. An alternative explanation is that most of the thermal energy $g\alpha u\theta$ is put into the largest scales through the wind so that the little remaining thermal input does not disturb the energy cascade which, therefore, follows the classical Kolmogorov scaling. According to the early model proposed by Grossman & Lohse (1991), the energy flux towards the small scales is constant and the observed Kolmogorov scaling of the velocity spectra is consistent (D. Lohse, personal communication).

Different behaviours are observed at Ra larger than 2×10^{10}. An example of the temperature spectra obtained at $Ra = 2 \times 10^{11}$ both in the bulk and close to the lateral

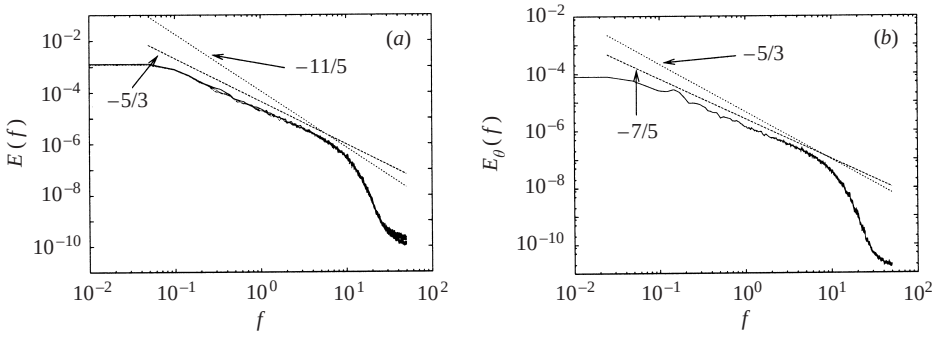

FIGURE 25. (*a*) Velocity and (*b*) temperature spectra in the bulk (all the probes with $0.4 \leqslant x/h \leqslant 0.6$ and $r/h \leqslant 0.1$) $Ra = 2 \times 10^{10}$. The Bolgiano and Kolmogorov slopes are reported for comparison.

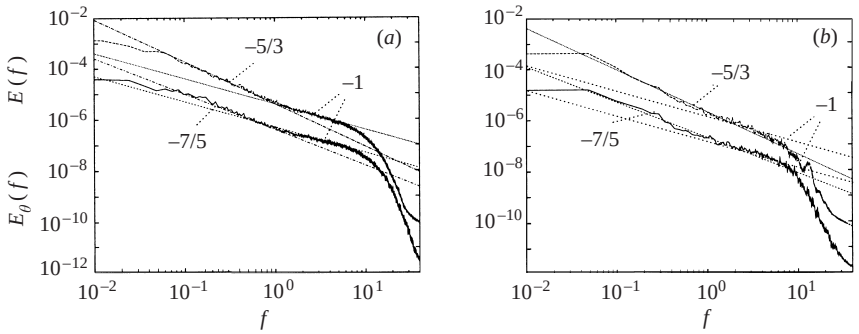

FIGURE 26. Comparison of the velocity and temperature spectra (*a*) in the bulk and (*b*) close to the sidewalls at $Ra = 2 \times 10^{11}$.

wall (halfway between the plates) is reported in figure 26. We note that due to the larger number of virtual probes, the spectrum computed in the homogeneous region is smoother than the non-homogeneous one, indicating a greater statistical accuracy. This means that the high-frequency peaks observed in the 'wall' spectrum are spurious effects related to the lack of statistical convergence. On comparing figure 26 with the analogous results obtained at lower Ra, a broadening of the power law decay range towards both low and large frequencies is seen. In the vicinity of the transitional region between the inertial and the dissipative ranges, the generation of a 'bump' is observed which appears to be more pronounced in the homogeneous region than in the wall region. As noted in figure 26 the generation of the bump is sensed also by the velocity fluctuation spectra. It is also evident that, independently from the presence of the bump, velocity and temperature behaviours are still quite different and, according to previous results at lower Ra, the first is dominated by the Kolmogorov dynamics and the latter by the Bolgiano scaling, consistently with the results of figure 22. The presence of a bump in the region separating the power law decay range from the dissipative range has also been observed in experiments on convective turbulence. Examples are reported in figures 27 and 28 where the spectra obtained from present numerical simulation at $Ra = 2 \times 10^{11}$ are compared with experimental results obtained in a cell geometry identical to the present one (J. Niemela, personal communication) for $Pr = 0.7$ and $Ra \simeq 1.6 \times 10^{11}$. The presentation of the spectra in compensated form (figures 27*c*, *d* and 28*c*, *d*) makes clearer the presence of the bump both in the homogeneous region in the bulk (figure 27) and close to the sidewalls (figure 28) and the agreement between experiments and numerical results is fairly good.

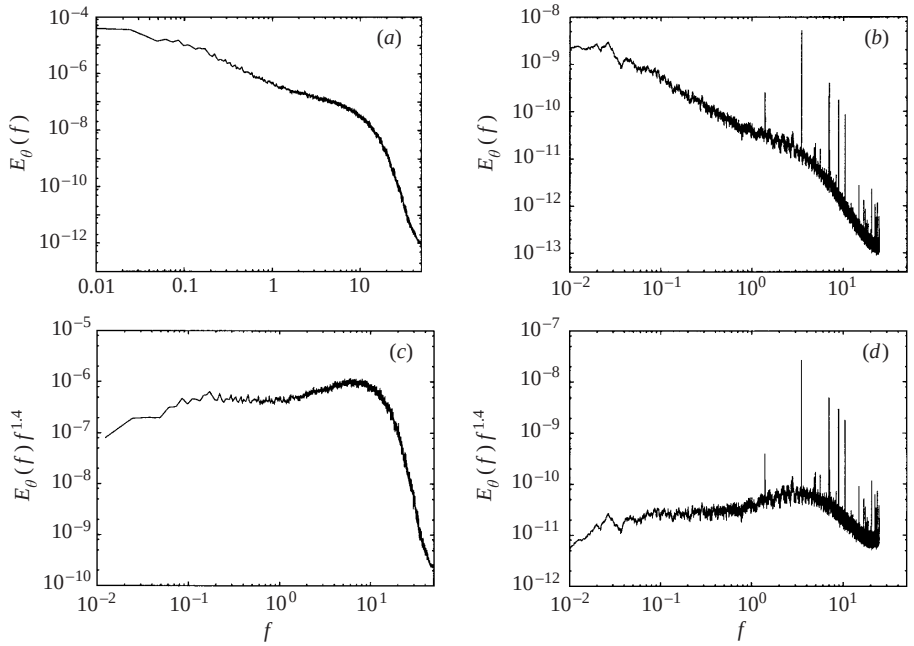

FIGURE 27. (a,c) Numerical and (b,d) experimental temperature spectra in the bulk and halfway between the plates at $Ra = 2 \times 10^{11}$ ($Ra \simeq 1.6 \times 10^{11}$ for the experiments). Panels (c) and (d) are compensated spectra. Experimental data by J. Niemela (personal communication).

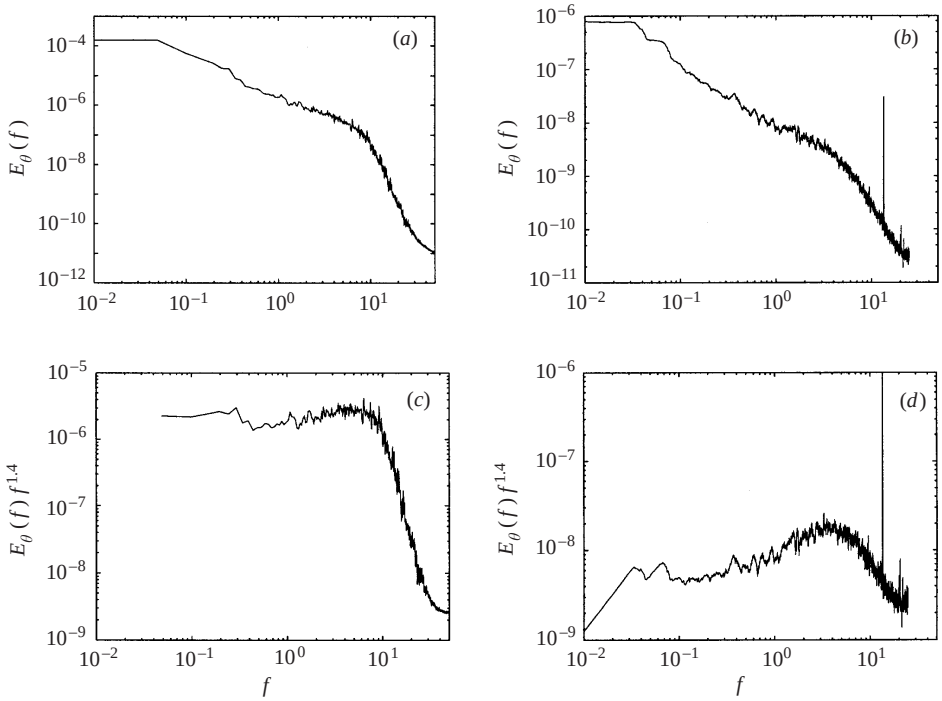

FIGURE 28. Numerical (a,c) and (b,d) experimental temperature spectra close to the sidewalls and halfway between the plates at $Ra = 2 \times 10^{11}$. Panels (c) and (d) are compensated spectra.

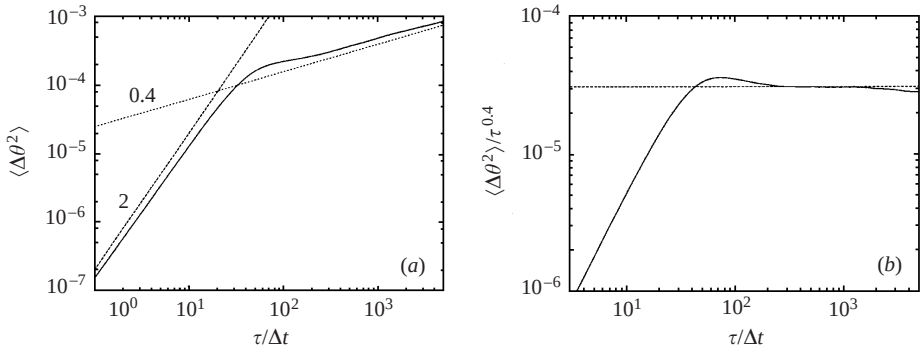

FIGURE 29. (*a*) Numerical temperature structure function in the bulk and halfway between the plates at $Ra = 2 \times 10^{11}$; (*b*) compensated spectra; straight lines are the slopes of the power laws reported for comparison.

Analogous features are observed in the physical domain as found from the analysis of the temperature structure functions computed from the present virtual probes. More specifically, we computed the second-order temperature structure function, defined as follows:

$$S_2(\tau) = \langle \Delta\theta^2(\tau) \rangle = \langle [\theta(t+\tau) - \theta(t)]^2 \rangle. \tag{3.2}$$

The angle brackets denote an averaging procedure which is performed both in time and by the ensemble average of the S_2 resulting from the set of probes belonging to the same region (bulk or wall). However, for clarity, the analysis of the time domain features is limited to the bulk probes since the smaller amount of available data in the wall region did not ensure a reliable estimation of S_2.

Examples of results obtained at $Ra = 2 \times 10^{11}$ within the homogeneous region are reported in figure 29. Panel 29(*a*) clearly shows the presence of a scaling law for large time separations (low frequencies) and, according to the spectral results, the scaling exponent in the time domain is very close to 0.4, thus leading to the observed $-7/5 = -1.4$ exponent in the frequency domain. It is also observed that at very small scale the temperature structure function follows a power law close to the form $S_2(\tau) \sim \tau^2$, indicating that the dissipative region has been well resolved by present simulation even at the largest Ra considered here. Figure 29(*b*) corresponds to the compensated structure function and in addition to confirming the Bolgiano scaling at relatively large scales, also indicates the presence of the bump in the region separating the Bolgiano scaling from the dissipation range.

It can be concluded that both numerical and experimental results clearly demonstrate that the presence of the bump observed at very large Ra in the region of frequency or time scales, which separates the power law range from the dissipation region, is a signature of real physical effects.

The physical explanation of such a behaviour is not straightforward. One possibility could be the occurrence of a 'bottle-neck' spectrum accumulation at small scales due to the excitation of high frequencies whose energy is not dissipated efficiently. This effect may be physically related to the presence in the mean flow of the two counter-rotating convective cells which, by driving fluid from the hot and cold plates directly into the cell centre, produce sharp temperature 'cliffs'. Since, as suggested above, temperature fluctuations are 'active' (and not driven by the velocity) they induce analogous phenomena in the velocity fluctuations. This idea is supported by the fact that the bump observed in the spectra presented above is much more evident in the bulk region than within the region of flow close to the lateral walls.

This scenario is further confirmed by the observation that a sharp cliff can be roughly represented by a Heaviside function whose spectrum decays like f^{-1}; this slope is that found in figure 26 where both the velocity and the temperature bumps are compared with a -1 exponent, showing a good agreement.

The main physical consequence of the above arguments is therefore that the presence of well-defined convective structures at large Ra can have consequences on the fluctuations in the bulk and on their spectra even at the smallest scales. This confirms the idea that the cell aspect ratio is an important parameter for the flow dynamics, not only concerning the large-scale features but also for the turbulence dynamics.

4. Closing remarks

In this study we have replicated, by numerical experiments, the flow investigated by Roche *et al.* (2001) and Niemela *et al.* (2000), sketched in figure 1. Taking advantage of the data accessibility provided by the direct numerical simulation the flow dynamics has been explored and separated into its mean large-scale and fluctuating components, both in the bulk and in the boundary layer regions. The existence of large-scale long-lived structures has been confirmed, although with a dynamics which is different from that conjectured from laboratory experiments. In fact, the presence of a single recirculation (similar to the $\Gamma = 1$ aspect-ratio flow) was observed only for $Ra < 10^9$–10^{10} and, given its reduced intensity, had marginal influence on the flow dynamics which, instead, was dominated by axisymmetric toroidal vortices attached to the horizontal plates. On the other hand, the latter structures, for $Ra > 10^{10}$, become less important than the bulk recirculation which breaks up into two counter-rotating asymmetric unity-aspect-ratio rolls. This transition has an appreciable impact on the boundary layer structure, on the statistics of the bulk turbulence and on the global heat transfer.

It is important to point out that the above feature is a peculiarity of this $\Gamma = 1/2$ aspect-ratio cell since a similar behaviour has not been observed by Verzicco & Camussi (1999), Cioni, Ciliberto & Sommeria (1997), Castaing *et al.* (1989), among many others, in $\Gamma = 1$ cells for a wide range of Rayleigh and Prandtl numbers. This should not be surprising when considering that, as observed by Daya & Ecke (2001) in $\Gamma = 1$ geometries, not only the aspect ratio (as shown in Kerr 2001), but also the cell shape (in that case cubic or cylindrical) can influence the statistics in the bulk.

Keeping in mind that low-aspect-ratio cells behave differently from other geometries we can briefly reconsider the results of the previous sections in the light of the Grossmann & Lohse (2000, 2001) theory which classifies different flow regimes in the Ra–Pr phase diagram in terms of the dominant contributions to the energy and temperature variance dissipations from the bulk and the boundary layers; we report in figure 30 their transitional map with the symbols indicating our set of simulations. According to the diagram there is a transition between the dominant regimes II_l–IV_l with a possible further transition towards IV_u for the last point.

Figure 18 confirms that a transition of the dominant contributions to the dissipation indeed occurs even though it is not of the right kind. In fact, region II_l pertains to flows with ϵ and N, respectively, coming essentially from the bulk and from boundary layers and $\delta_u \ll \delta_\theta$; in contrast, any point of region IV has both dissipations coming from the bulk.

Concerning the boundary layers we note from figure 15 that $\delta_\theta < \delta_u$ always holds, indicating a flow of the type II_u instead of II_l for $Ra \leqslant 10^9$. This, however, is only

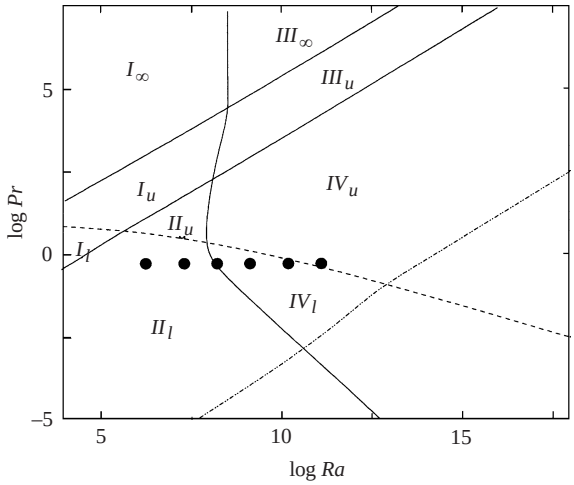

FIGURE 30. Grossmann & Lohse's phase diagram with the present numerical simulations (symbols). Assuming $\epsilon = \epsilon_{bu} + \epsilon_{bl}$ and $N = N_{bu} + N_{bl}$, *bu* denoting the bulk and *bl* the boundary layers, the different zones are divided according to: I, $\epsilon \simeq \epsilon_{bl}$ and $N \simeq N_{bl}$; II $\epsilon \simeq \epsilon_{bu}$ and $N \simeq N_{bl}$; III $\epsilon \simeq \epsilon_{bl}$ and $N \simeq N_{bu}$; IV $\epsilon \simeq \epsilon_{bu}$ and $N \simeq N_{bu}$; l and u, respectively, indicate regions where $\delta_\theta > \delta_u$ and $\delta_u > \delta_\theta$.

a minor mismatch since, as noted by Grossmann & Lohse (2000) the separations between the various regions should be considered more as indicative boundaries rather than strict thresholds. Nevertheless, while the difference between II_u and II_l could be easily remedied by shifting their boundary down, regions IV (with ϵ from the bulk and N from the boundary layers) are eventually crossed according to figure 30 while for the present flow the region II_u seems to be asymptotic (see figures 15 and 18), at least before the appearance of the ultimate regime $Nu \sim Ra^{1/2}$.

We believe that one possible explanation is found in the structure of the large-scale flow that, for this geometry, is not as simple as in larger-aspect-ratio cells. Indeed the diagram reported in figure 28 had been calculated for $\Gamma = 1$ cells, thus considering different structures of the large recirculation cells. In particular, we have shown that the cell slenderness and the no-slip sidewall modifies the strength and topology of the 'wind of turbulence' thus changing the balance of the dissipations. As an aside we note that the lateral no-slip adiabatic surface produces a viscous boundary layer while no thermal boundary layer is developed. This further confirms that the dissipation dynamics of figure 18 should not be attributed to the introduction of additional boundary layers but rather to the large-scale confinement that is in turn reflected in the boundary layer and bulk evolutions.

A confirmation of the aspect-ratio influence is given by the data of Verzicco & Camussi (1999) simulating turbulent convection in a cylindrical cell of aspect ratio $\Gamma = 1$ at $Pr = 0.7$. In that case, viscous and thermal boundary layer thicknesses were found to decrease at a different rate with increasing Rayleigh and a cross-over with $\delta_\theta > \delta_u$ for $Ra < 2 \times 10^7$ and $\delta_u > \delta_\theta$ for $Ra > 2 \times 10^7$ was observed. Although the transitional Rayleigh number is considerably different from that indicated in figure 30 the trend is correct since a straight line drawn at $Pr = 0.7$ initially crosses l-subscript regions and eventually ends up in u-subscript zones.

A deeper comparison should also involve the balances of the dissipations and possibly larger-aspect-ratio geometries in order to verify whether the aspect ratio

effect decreases with increasing Γ and whether a threshold value exists. Since these different dynamics result in different Nu vs. Ra relationships, this aspect deserves more investigation and it will be the topic for a future study.

A final word of warning should be given about the observed change of scaling for the highest values of Ra. In fact, the present results showed a transition in the mean flow structure and in the heat transfer for $10^9 \leqslant Ra \leqslant 10^{10}$ while, on the other hand, our available computers allowed us to perform reliable simulations 'limited' to $Ra \leqslant 2 \times 10^{11}$. This implies that any claim about the transition relies only on observations on one decade in Ra ($2 \times 10^{10} \leqslant Ra \leqslant 2 \times 10^{11}$) without evidence about the persistence of this change to higher Ra. In addition, as explained in § 2, we cannot capture by direct numerical simulations all the very low-frequency phenomena related to the mean wind reversal observed by Niemela *et al.* (2001); therefore there might be the possibility that the observed transition is a temporary change associated with the formation of the new structure and that at still higher Ra the original scaling appears again.

We wish to thank Dr J. Niemela, Dr F. Chillà and Dr B. Castaing for fruitful discussions and for providing some experimental data. The simulation at the highest Rayleigh was possible thanks to the computer facilities of CASPUR (Consorzio interuniversitario per le Applicazioni di Supercalcolo Per Università e Ricerca). Drs F. Massaioli and G. Amati are gratefully acknowledged for the technical support in implementing openMP and using parallel computers.

REFERENCES

Ashkenazi, S. & Steinberg, V. 1999 High Rayleigh number turbulent convection in a gas near the gas-liquid critical point. *Phys. Rev. Lett.* **83**, 3641–3644.

Belmonte, A., Tilgner, A. & Libchaber, A. 1994 Temperature and velocity boundary layers in turbulent convection. *Phys. Rev.* E **50**, 269–279.

Camussi, R. & Verzicco, R. 1999 Turbulent convection in mercury: scaling laws and spectra. *Phys. Fluids* **10**, 516–527.

Castaing, B., Gunaratne, G., Heslot, F., Kadanoff, L., Libchaber, A., Thomae, S., Wu, X. Z., Zaleski, S. & Zanetti, G. 1989 Scaling of hard thermal turbulence in Rayleigh-Bénard convection. *J. Fluid Mech.* **204**, 1–30.

Chavanne, X., Chillà, F., Chabaud, B., Castaing, B. & Hebral, B. 2001 Turbulent Rayleigh-Bénard convection in gaseous and liquid He. *Phys. Fluids* **13**, 1300–1320.

Ciliberto, S., Cioni, S. & Laroche, C. 1996 Layer-scale flow properties of turbulent thermal convection. *Phys. Rev.* E **54**, 5901–5905.

Cioni, S., Ciliberto, S. & Sommeria, J. 1997 Strongly turbulent Rayleigh-Bénard convection in mercury: comparison with results at moderate Prandtl number. *J. Fluid Mech.* **335**, 111–140.

Daya, Z. A. & Ecke, R. E. 2001 Does turbulent convection fell the shape of the container? *Phys. Rev. Lett.* **89**, 4501, U81–U83.

Glazier, J. A., Segawa, T., Naert, A. & Sano, M. 1999 Evidence against ultra hard thermal turbulence at very high Rayleigh numbers. *Nature* **398**, 307–310.

Grossmann, S. & Lohse, D. 1991 Fourier–Weierstrass mode analysis for thermally driven turbulence. *Phys. Rev. Lett.* **67**, 445–448.

Grossmann, S. & Lohse, D. 2000 Scaling in thermal convection: a unifying theory. *J. Fluid Mech.* **407**, 27–56.

Grossmann, S. & Lohse, D. 2001 Thermal convection for large Prandtl numbers. *Phys. Rev. Lett.* **86**, 3316–3319

Grötzbach, G. 1983 Spatial resolution requirements for direct numerical simulation of the Rayleigh-Bénard convection. *J. Comput. Phys.* **49**, 241–264.

Heslot, F., Castaing, B. & Libchaber, A. 1987 Transition to turbulence in helium gas. *Phys. Rev.* A **36**, 5870–5873.

Jiménez, J., Wray, A. A., Saffman, P. G. & Rogallo, R. S. 1993 The structure of intense vorticity in isotropic turbulence. *J. Fluid Mech.* **255**, 65–90.

Kerr, R. 1996 Rayleigh number scaling in numerical convection. *J. Fluid Mech.* **310**, 139–179.

Kerr, R. 2001 Energy budget in Rayleigh–Benard convection. *Phys. Rev. Lett.* **87**, 4502, U69–U71.

Kraichnan, R. H. 1962 Turbulent thermal convection at arbitrary Prandtl number. *Phys. Fluids* **5**, 1374–1389.

Monin, A. S. & Yaglom, A. M. 1975 *Statistical Fluid Mechanics*, vol. 2. MIT Press.

Niemela, J. J., Skrbek, L., Sreenivasan, R. R. & Donnely, R. J. 2000 Turbulent convection at very high Rayleigh numbers. *Nature* **404**, 837–841.

Niemela, J. J., Skrbek, L., Sreenivasan, K. R. & Donnely, R. J. 2001 The wind in confined thermal convection. *J. Fluid Mech.* **449**, 169–178.

Pope, S. B. 2000 *Turbulent Flows*. Cambridge University Press.

Roche, P. E., Castaing, B., Chabaud, B. & Hebral, B. 2001 Observation of the 1/2 power law in Rayleigh-Bénard convection. *Phys. Rev.* E **63**, 045303-1–045303-4.

Shraiman, B. I. & Siggia, E. D. 1990 Heat transport in high Rayleigh number convection. *Phys. Rev.* A **42**, 3650–3653.

Siggia, E. D. 1994 High Rayleigh number convection. *Annu. Rev. Fluid Mech.* **26**, 137–168.

Sreenivasan, K. R., Bershadskii, A. & Niemela, J. J. 2002 Mean wind and its reversal in thermal convection. *Phys. Rev.* E **65**, 056306.

Swartzrauber, P. N. 1974 A direct method for the discrete solution of separable elliptic equations. *SIAM J. Numer. Anal.* **11**, 1136–1150.

Verzicco, R. & Camussi, R. 1997 Transitional regimes of low-Prandtl thermal convection in a cylindrical cell. *Phys. Fluids* **9**, 1287–1295.

Verzicco, R. & Camussi, R. 1999 Prandtl number effects in convective turbulence. *J. Fluid Mech.* **383**, 55–73.

Verzicco, R. & Orlandi, P. 1996 A finite-difference scheme for three-dimensional incompressible flow in cylindrical coordinates. *J. Comput. Phys.* **123**, 402–413.

Wu, X. Z. 1991 Along a road to developed turbulence: free thermal convection in low temperature helium gas. PhD Thesis, University of Chicago.

Wu, X. Z., Kadanoff, L., Libchaber, A. & Sano, M. 1990 Frequency power spectrum of temperature fluctuations in free convection. *Phys. Rev. Lett.* **18**, 2140–2143.

Wu, X. Z. & Libchaber, A. 1992 Scaling relations in thermal turbulence: The aspect-ratio dependence. *Phys. Rev.* A **45**, 842–845.